ORIGINAL RESEARCH ARTICLE

The Depositional Record
A journal of the International Association of Sedimentologists

WILEY

The Early–Middle Miocene climate as reflected by a mid-latitude lacustrine record in the Ebro Basin, north-east Iberia

Concha Arenas[1,2,3] | Cinta Osácar[1,2,3] | Francisco Javier Pérez-Rivarés[1] | Joaquín Bastida[4] | Andrés Gil[1,2,3] | Luis F. Auqué[1]

[1]Department of Earth Sciences, University of Zaragoza, Zaragoza, Spain

[2]Institute for Research on Environmental Sciences of Aragón (IUCA), Zaragoza, Spain

[3]Geotransfer Group, University of Zaragoza, Zaragoza, Spain

[4]Unit of Geology, University of Valencia, Valencia, Spain

Correspondence
Concha Arenas, Área de estratigrafía, Dpto. Ciencias de la Tierra, Universidad de Zaragoza, C/Pedro Cerbuna 12, Zaragoza 50009, Spain.
Email: carenas@unizar.es

Abstract

This contribution examines the climate variations reflected by a mainly lacustrine succession spanning from 17.73 to 14.0 Ma in north-east Iberia, thus encompassing the Miocene Climatic Optimum (MCO). The study is based on the δ^{13}C and δ^{18}O composition of an array of carbonate facies and marl samples, complemented with sedimentological analysis, illite crystallinity index and magnetic susceptibility data. The onset and ending of the MCO have been detected at *ca* 17.10-17.06 Ma and 14.56 Ma, roughly equivalent to the boundaries in the marine record, although with relatively short lags. The variability of the data series evidenced changes in humidity and air temperature through the MCO, some of which coincided with similar variations in other records. Specifically, an evolving positive shift in δ^{13}C values, from 16.5 to 14.5 Ma, seems to fit the Monterey excursion observed in marine records. Likewise, increases in δ^{18}O values between 16.8 and 16.5 Ma and between 14.85 and 14.56 Ma in the study succession concurred with warming intervals recorded in palaeosols of Central Europe, emphasising the coincidence with the temperature maximum at *ca* 16.6 Ma. A general decline in temperature and an increase in humidity are detected from 14.56 Ma, both with steeper trends until 14.41 Ma then more gradual onwards, indicating the beginning of the Middle Miocene Climatic Transition. These results shed light upon the tightly coincidental features between terrestrial and marine records over those time intervals and, more importantly, highlight the earlier warming and the faster cooling experienced by the lake system as compared with the marine record. These findings provide further evidence to help infer palaeoclimate conditions on a much broader reach than the regional context.

1 | INTRODUCTION

The lack of precise chronological data and often discontinuous character of some continental records have constrained the accurate study of not a few climate-related milestones in the Earth's history, for example, some phenomena during the Cenozoic based on lacustrine deposits, when compared with the more numerous studies in the marine realm. One of the debated milestones concerns the Miocene Climatic Optimum (MCO), the most recent, prolonged global warming period in the Earth's history. The boundaries of the MCO are set from the marine sedimentary record between approximately 17 Ma and 15-14 Ma, depending on the authors (Holbourn et al., 2007; Westerhold et al., 2020; Zachos et al., 2001, 2008). Collectively, it has been characterised by the increase in temperature and humidity within a span of progressive cooling through the Neogene (Böhme, 2003). The short cooling period that follows the MCO is named the Middle Miocene Climatic Transition (MMCT) by some authors (Mourik et al., 2010; Westerhold et al., 2020).

Regarding the marine record, many palaeoclimate studies are based on information derived from foraminifera and other micro-biota, primarily using C and O stable isotopes of benthic foraminifera, in well dated sections (Holbourn et al., 2018; Steinthorsdottir et al., 2020; Westerhold et al., 2020; Zachos et al., 2001, among many others). In contrast to the numerous available marine records, continental palaeoclimate data from the MCO and the subsequent MMCT are poorly documented, mainly due to the frequent depositional hiatuses (Sun & Zhang, 2008) and lack of appropriate deposits with precise dating. Therefore, the characteristics of the beginning and ending of the MCO and their timing are not so well known in the continental record.

A variety of specific studies concerning palaeosols (Methner et al., 2020; Oerter et al., 2016; Sheldon, 2006) and diverse palaeobotany proxies, such as plant taxa (Kürschner et al., 2008; Pound et al., 2012; Zheng et al., 2019) and pollen (Sun & Zhang, 2008; Widera et al., 2021), together with other multidisciplinary studies on lake deposits (Grygar et al., 2017; Mandic et al., 2011), strongly indicate climate changes on both local and global scale during and close to the MCO interval. Additionally, the alteration index from clay minerals (Song et al., 2018 and references therein) or the lake sediment organic geochemistry (Lebreton-Anberrée et al., 2016 and references therein) have been used to establish short climate fluctuations during the MCO.

In the Ebro Basin, in the north-east of the Iberian Peninsula (Figure 1A), a well-exposed lacustrine and distal alluvial record with available chronology, contrasted through magnetostratigraphy and biostratigraphy (Agustí et al., 2011; Pérez-Rivarés et al., 2018), provides the opportunity to explore in detail the characteristics of the MCO record, as well as the underlying and overlying deposits.

The only known study in the Ebro Basin (western central area) having robust chronological data that deal with the lower portion of the MCO time interval is based on microvertebrates, ostracods and charophytes (Suarez-Hernando, 2017). This author reported an overall increase in temperature starting *ca* 2 Ma earlier than in the marine record, and an increase in humidity at *ca* 16 Ma (Larena et al., 2020; Suarez-Hernando, 2017).

The characteristics of the lacustrine and associated continental sedimentary records are greatly dependent on a combination of parameters that are linked to tectonics and climate (Bohacs et al., 2000, 2007; De Wet et al., 1998; Vázquez-Urbez et al., 2013). Tectonics may cause changes in basin development and lake hydrology through time due to modifications of the topography (e.g. relief rejuvenation and the allied sediment supply) and drainage patterns both in the catchment and in basin areas (Davis et al., 2009). Climate and climate-related parameters (temperature, precipitation, evaporation and the development of fauna and flora, i.e. vegetated covers), both in the catchment and in basin areas, for example, the lake system, can strongly influence variations in the lake water level and the type and amount of sediment supply to the lake basin (Alonso-Zarza et al., 2012; Arenas & Pardo, 1999; Carroll et al., 2006; De Wet et al., 1998). For example, weathering and denudation in the catchment and nearby basin areas strongly depend on relief, precipitation and temperature (Einsele, 2000). Changes in the magnitude or intensity of all these parameters through time can be reflected by a variety of proxies that include sedimentary facies and facies associations on diverse timescales, and geochemical, mineralogical, magnetic, and biological characteristics of the lake deposits. All these parameters complement each other and can provide reliable information on climate variations over diverse timescales.
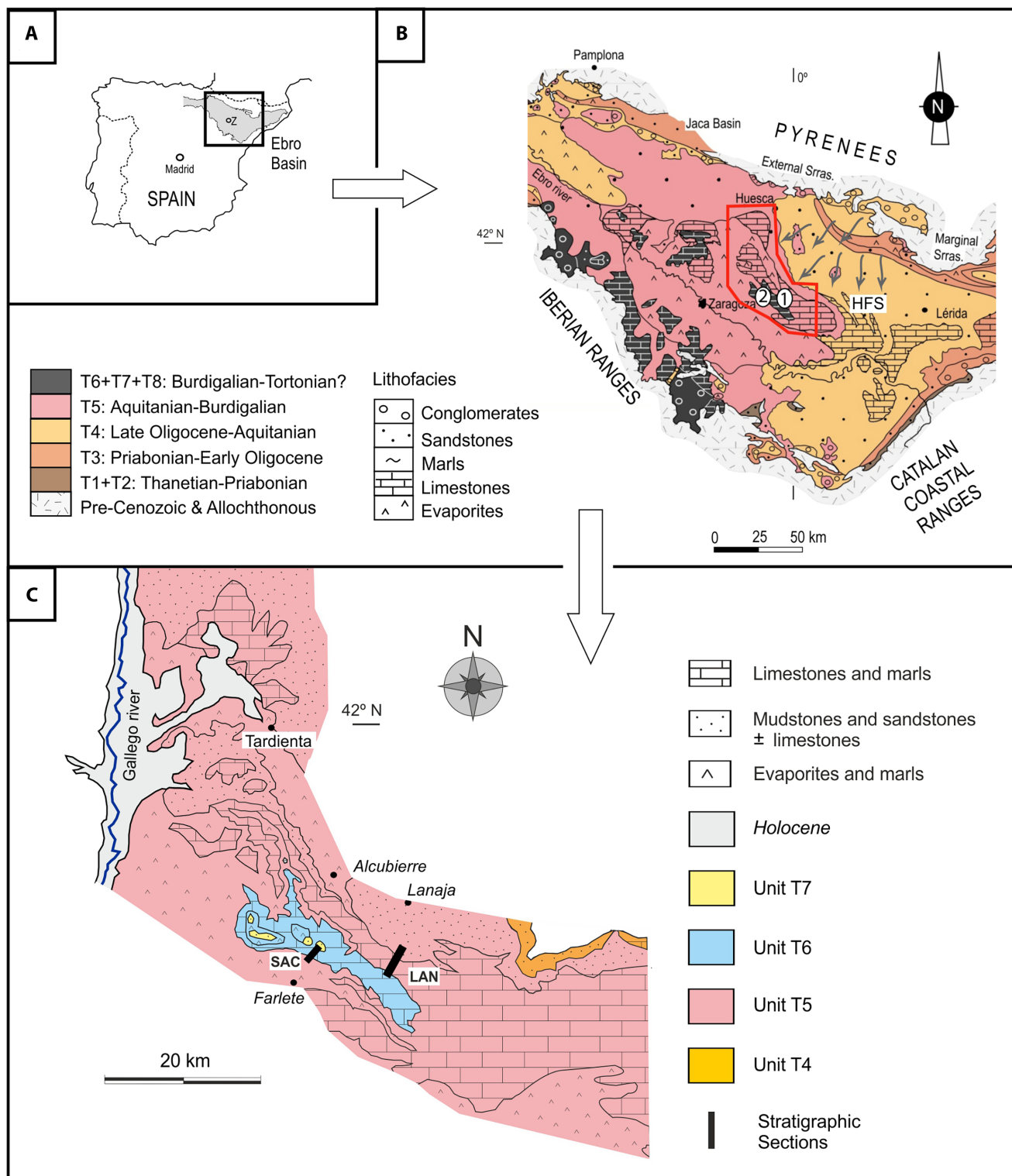
FIGURE 1 (A) Location map of the Ebro Basin in the north-east of the Iberian Peninsula. (B) Map showing the distribution of genetic stratigraphic units (Tecto-Sedimentary Units) described in the Ebro Basin (adapted from Muñoz et al., 2002). 1, Lanaja section; 2, San Caprasio section. Arrows show the location and flow direction of the Huesca fluvial system (HFS; Nichols & Hirst, 1998). (C) Simplified geological map with genetic stratigraphic units and lithofacies of the Sierra de Alcubierre (modified from Arenas & Pardo, 1999). LAN, Lanaja section; SAC, San Caprasio section.

The $\delta^{13}C$ and $\delta^{18}O$ composition of lacustrine and palustrine carbonate sediments has been shown to reflect climate and climate-related parameters that affect lake systems and their catchments (Alonso-Zarza et al., 2012; Hammarlund et al. 2003; Kelts & Talbot, 1990; Leng & Marshall, 2004). Likewise, chemical alteration indexes

from lacustrine and palustrine deposits are also important proxies for climate reconstruction, for example, to infer the intensity of climate-related parameters affecting the sediment source areas, such as physical and chemical weathering, precipitation and temperature. In this context, the illite crystallinity index has been used as a proxy for chemical weathering, through mineral hydrolysis, and therefore, surface air humidity (Arkai, 1993; Jaboyedoff et al., 2001; Thorez, 1989). Previous studies have shown the utility of this proxy in palaeoclimate studies of Miocene marine sediments (He et al., 2022; Ma et al., 2023) and continental successions (Wang et al., 2020), including lake deposits (Zeng et al., 2014). The illite crystallinity index has also been used in studies investigating the sediment source areas of the studied successions, for example, the Graus and Tremp basins (Arostegi et al., 2011; Bastida et al., 2017).

Other parameters used to indirectly inform on climate variations are the magnetic properties of some minerals, for example, magnetic susceptibility (MS). Magnetic grains can act as highly sensitive markers of palaeoclimate and palaeoenvironmental changes (Maher & Thompson, 1999). The origin and post-depositional history of these grains can vary the concentration of magnetic minerals in the sedimentary record. The MS is used as an indicator of detrital sediment supplied to a basin which is related to changes in the catchment area that are often linked to climate (Ellwood et al., 2000; Geiss et al., 2003; Mandic et al., 2011).

This contribution focusses on obtaining refined palaeoclimate information from a sedimentary record in the Ebro Basin using available stratigraphic, sedimentologic, palaeogeographical and chronologic information. The objectives include: (1) to deduce the climate characteristics of the beginning and ending of the MCO through the stable isotope composition ($\delta^{13}C$, $\delta^{18}O$) of carbonate lacustrine and distal alluvial deposits in a mid-latitude region, setting the significant changes through time; (2) to complement these results with those gathered from the illite crystallinity index and MS data of the same sections; (3) to compare the results with information provided by other terrestrial and marine records and discuss the characters of climate evolution and the timing offset of these changes.

By examining the climate variations reflected by a mainly lacustrine succession through the MCO, this contribution sheds light upon coincidental and differential features between terrestrial and marine recordings, including timing of outset and end of milestones or significant points in climate evolution, such as the Monterey event. These results may help further research to delve into the possible causes on a broader reach.
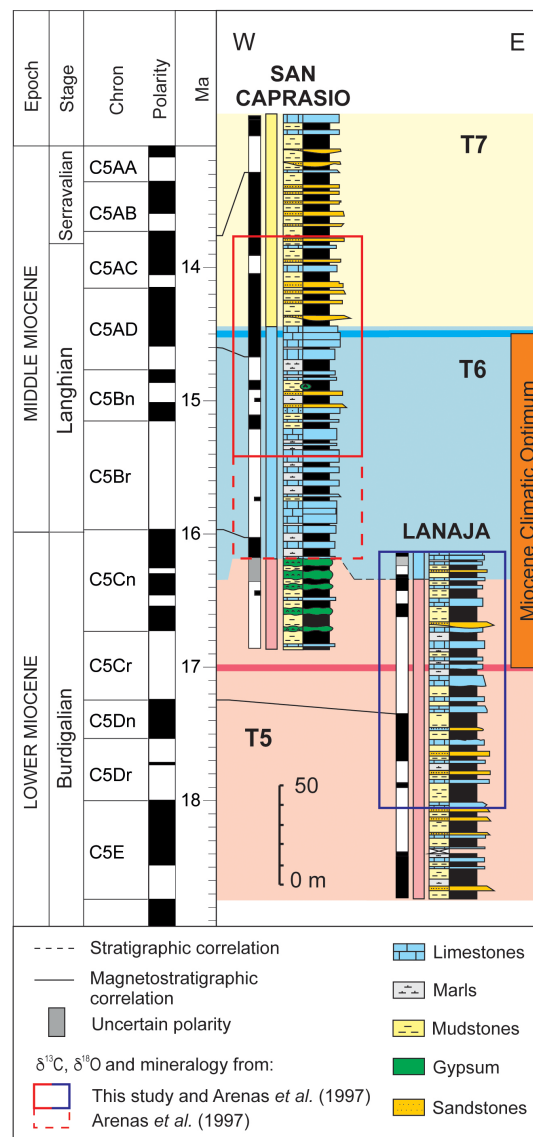
FIGURE 2 Stratigraphic and magnetostratigraphic correlation of the Lanaja and San Caprasio sections in the Sierra de Alcubierre area and genetic stratigraphic units T5, T6 and T7 (based on Arenas, 1993; Arenas & Pardo, 2000; Pérez Rivarés et al., 2018). MCO span from several authors (Steinthorsdottir et al., 2020; Zachos et al., 2001). GPTS, Geomagnetic Polarity Time Scale. Absolute ages for epochs, stages and geomagnetic polarity from Ogg (2020).

2 | STRATIGRAPHIC, SEDIMENTOLOGICAL AND PALAEOGEOGRAPHICAL CONTEXT

The study area—Sierra de Alcubierre—is formed of up to *ca* 600 m thick distal alluvial siliciclastic and lacustrine carbonate and sulphate deposits that formed during the Early to Middle Miocene in the central Ebro Basin, northeast Iberia (Figure 1A). Three genetic stratigraphic units (named T5, T6 and T7; Arenas, 1993; Muñoz et al., 2002)

crop out in the Sierra de Alcubierre (Figures 1B,C and 2). In this area, the 370 m thick unit T5 mostly consists of gypsum, mudstones, dolostones and marlstones, passing laterally to the north and east to limestones and marls. Unit T6, which is 120 m thick here, is formed dominantly of limestones and marlstones, with occasional dolostones, mudstones and sandstones, and a gypsum-rich wedge at the upper portion. This evaporite-rich wedge corresponds to the Perdiguera Member as defined by Arenas (1993) and Arenas and Pardo (1999). Mudstones, marlstones, sandstones and limestones make up the younger unit (T7) in the study area, reaching thicknesses of up to 107 m (this record represents approximately the lower half of the unit; the complete unit crops out to the south-west of the study area). Magnetostratigraphic studies have dated these units to between 21.3 Ma and 13.5 Ma and estimated their duration as follows: 5.4 Ma for T5, 2.2 Ma for T6 and at least 0.9 Ma for T7 (Pérez Rivarés, 2016; Pérez-Rivarés et al., 2018). The boundaries between these units in the studied area have been shown to be nearly synchronous, with differences ranging between 40 ka and 280 ka (Pérez-Rivarés et al., 2018).

The sediment source area of units T5, T6 and T7 in the Sierra de Alcubierre was located in the south Pyrenean central unit, including the Pyrenean Eocene ± Oligocene basins, the Maastritchtian to Palaeocene Internal Sierras, and further north the Axial Zone of the Pyrenees (Figure 1B). The Huesca fluvial system (HFS in Figure 1B; named by Hirst & Nichols, 1986) was a distributary system that originated in the aforementioned zones and sourced the central lacustrine system, where the studied rocks formed. The outcropping deposits of this fluvial system are limited to the pre-T6 record. Sedimentological and mineralogical studies of units T5, T6 and T7 in the Sierra de Alcubierre indicated that these units were sourced by the same Pyrenean zones (Arenas & Pardo, 1999).

2.1 | Sedimentological context

Siliciclastic mudstones and sandstones, marlstones, a wide variety of limestone and dolostone facies, and sulphate facies formed in distal alluvial plains and in lake systems within the study area. Based on the lithology and sedimentary structures, the following sedimentary facies are distinguished (Arenas, 1993): sandstones (S), mudstones (F), marls and marlstones (M), laminated limestones and dolostones (Ll; either with ripples, hummocky cross-stratification or horizontal lamination), stromatolitic limestones and dolostones (Ls), massive bioclastic limestones and bioturbated bioclastic limestones (Lm, Lb). Sulphate facies include rippled, laminated, nodular,

macrocrystalline and lenticular gypsum (Gr, Gl, Gn, Gmac, Gln). Their main features and depositional interpretation are summarised in Table 1 and illustrated in Figures 3 and 4. The sedimentary facies model for lacustrine deposition during units T5, T6 and base of T7 (Figure 5) suggests that lake water-level variations and hydrodynamics (e.g. surge activity) controlled the formation of the different carbonate and sulphate sediments and a variety of overprinting features through time (Arenas & Pardo, 1999).

Based on sedimentological, mineralogical and stable isotope analyses, previous studies suggested an evolution toward decreasing aridity from unit T5 to T6, as evidenced by the change from dominant saline deposits to dominant freshwater lacustrine deposits (Arenas et al., 1997). The available sedimentological and palaeogeographical data indicate that the lacustrine system migrated southward as a result of Pyrenean thrusting since deposition of unit T5 onwards. Within this shift, unit T7 represents a sudden progradation of the Pyrenean fluvial system over the freshwater carbonate lacustrine system of unit T6 (Arenas & Pardo, 2000).

3 | MATERIALS AND METHODS

3.1 | The stratigraphic succession

Hard and soft sediment samples for textural, $\delta^{13}C$ and $\delta^{18}O$, bulk mineralogy and clay-mineralogy analyses were collected through two sections (Figures 1B,C and 2): Lanaja (LAN) and San Caprasio (SAC). These sections offer an almost continuous sedimentary record through the Burdigalian to the early Serravalian, using dating determined by the magnetostratigraphical studies of Pérez Rivarés (2016) and Pérez-Rivarés et al. (2018). The interval from 17.80 to 14.0 Ma was selected for this study. The ages of diverse time spans and samples within these sections have been estimated from this magnetostratigraphical record by interpolation within every chron. Based on the depositional rates calculated by Pérez Rivarés (2016), the *ca* 185 ka gap in stable isotope information represents a thickness of approximately 13 m between the last sample of section LAN and the first sample of section SAC (see Figure 7 below).

3.2 | Sampling and analytical techniques

Sampling in sections LAN and SAC was focussed on two intervals embracing the beginning and end of the MCO (Figure 2): (1) the lower interval, from 17.72 to 16.30 Ma in LAN, and (2) the upper interval, from 16.12 to 14.0 Ma in SAC. Mudstones, marls, marlstones and

TABLE 1 Main characteristics and depositional interpretations of sedimentary facies in this study. Summarised from Arenas et al. (1997) and Arenas and Pardo (1999).

Facies	Subfacies	Texture	Physical sedimentary structures & geometry	Biological & diagenetic features & components	Interpretation
Marls: M	Laminated marls		Horizontal lamination or lenticular stratification	CD	Settle-out, mostly in offshore lake areas, linked to runoff periods
	Structureless (massive) marls		None	Moll, Ostr, Char, CD, RBiot	
Laminated limestones and rare dolostones: L1	L11 / L12 / L13	Micrite and dolomicrite with mm to cm detrital laminae and lenses	L11: Lenticular or wavy stratification / L12: Horizontal lamination / L13: Hummocky cross stratification	Associated stromatolites	Wave influence above or below storm surge level / Shore sheet flows or inner turbidite-like currents (L12) / Moderate salinity waters
Stromatolitic and rare oncolitic limestones (rare dolostones): Ls	Planar layers / Bioherms / Biostromes	Boundstones	Microscopic alternations of light and dark dense micrite and light porous microspar laminae	Rod and coccoid calcite bodies / Rare filament algae and fungi	Shallow/marginal lacustrine areas / Moderate salinity waters
Bioclastic limestones	Structureless (massive): Lm	Mudstones and wackestones	Uncommon and poor lamination	Moll, Ostr, Char, CD / If present, weak bioturbation	Fresh water, shallow lacustrine areas / Permanent water supply
	Bioturbated: Lb / Depending on diagenetic processes	Mudstones and wackestones	Desiccation cracks	Moll, Ostr, Char, CD, Rbiot / Nodules, breccias	Palustrine conditions. Shallowing of previous fresh water lake areas
Nodular: Gn, and Macrocrystalline gypsum: Gmac		Microcrystalline (alabastrine) / Macrocrystalline	Nodules, forming beds or isolated / Discontinuous beds, rosettes	Nodules and grouped macrocrystals within previous deposits	Evaporative processes in saline mud flats / Gmac: later growth, e.g. from finer gypsum textures
Lenticular gypsum: Gln		Lenticular crystals	Rarely forming laminae		Gypsum precipitation in water lake and interstitially within the sediment
Rippled and Laminated Gypsum: Gr, Gl		Microcrystalline (alabastrine) and granular	Horizontal, lenticular and rippled lamination		Gypsum precipitation in hypersaline lake water
Halite: H		Cubic and chevron	Massive beds and hoppers	Gypsum and anhydrite pseudomorphs within mudstones, marls and L1	Precipitation of NaCl in very shallow salinas. Evaporative processes in saline mud flats
Mudstones: F	Fg: green, grey / Fo: ochre, orange		Structureless or with horizontal lamination	Mottling. Moll, Ostr, Char, CD, Rbiot	Nearshore lake areas or alluvial plains surrounding lacustrine areas
Sandstones: Sm, Sh, Sr, St			Structureless. Horizontal and ripple lamination, and trough-cross stratification	CD, Rbiot	Sheet flows and channels in alluvial plains, and within the lake areas

Abbreviations: CD, carbonaceous debris; Char, charophytes; Moll, molluscs; Ostr, ostracods; Rbiot, root traces or bioturbations *sl*.

limestones and dolostones were sampled for different purposes (Tables S1 and S2).

A minimum of 250 thin sections were prepared for sedimentological characterisation from the carbonate samples. The corresponding rock slabs were used to sample for $\delta^{13}C$ and $\delta^{18}O$ analyses. The soft samples were studied with the aid of a stereomicroscope. Thin sections and images were obtained from *Servicios de Apoyo a la Investigación* (SAI) of the University of Zaragoza, Spain. Observations and images were obtained using a petrographic microscope, an Olympus AX-70, coupled with a digital photography camera, an Olympus E-330.

3.3 | Mineralogy

The bulk mineralogical composition of 111 samples was determined by powder X-ray diffraction (P-XRD; results in Table S2) using samples ground and sieved to 53 μm prior to analysis. The analyses were performed (a) at the University of Zaragoza, using a Phillips PW 1729 diffractometer, equipped with a graphite monochromator and Cu-Kα radiation; (b) at Scientific Services (SCSIE) of the University of Valencia, in a Bruker D8 Advance A25 diffractometer, with linear focus Cu radiation and LYNXEYE XE 1-D detector, working at 40 kV and 30 mA; data evaluation and identification were performed with different applications of the EVA program from Bruker AXS. The criteria of Warshaw and Roy (1961) were used for identification of phyllosilicates. Semi-quantitative estimates were carried out by the RIR method according to Davis and Smith (1989).

In mudstones and marlstones (71 samples), the illite crystallinity index as full width at half maximum value (FWHM) was determined. The FWHM of the 001 reflection (*ca* 10 Å) was measured in diffraction patterns of normal oriented aggregates of the clay fraction. Analyses were carried out at Scientific Services (SCSIE) of the University of Valencia.

3.4 | Stable isotope analysis ($\delta^{13}C$ and $\delta^{18}O$)

A total of 107 marls and marlstones, carbonate mudstones, limestones and dolostones were prepared for $\delta^{13}C$ and $\delta^{18}O$ analyses (results in Table S1). Marls, marlstones and mudstones were carefully selected with aid of a stereomicroscope to avoid impurities, then ground and sieved to 53 μm. Hard-rock carbonate samples were selected from the same tablets used for thin section preparations, using a 0.5-mm diameter micro-drill powered by a micromotor (Navfram model N120 Micromotor 25,000 rpm

with an electronic speed regulator, AB SHOT TECNICS SL, Cervello, Barcelona, Spain). The device was coupled with a stereomicroscope, which helped in the selection of samples minimally affected by cements, recrystallisation or fossils (also determined in thin section). Powdered samples (0.2–0.5 mg) were stored in glass vials.

The $\delta^{13}C$ and $\delta^{18}O$ ratios were determined using a mass spectrometer (MAT-252, Thermo Finnigan; Thermo Fisher Scientific, Waltham, MA, USA) at Servicios Científico-Técnicos (CCIT-UB Serveis) of the University of Barcelona (Spain). The values were measured via CO_2 obtained in a Carbonate Kiel Device III (Thermo Finnigan) by the reaction of samples with 100% H_3PO_4 at 70°C for 3 min (McCrea, 1950). The international standard NBS-19 ($\delta^{13}C_{VPDB} = +1.95‰$ and $\delta^{18}O_{VPDB} = −2.20‰$) was used to calibrate $\delta^{13}C$ and $\delta^{18}O$ to the Vienna Pee-Dee Belemnite (VPDB). The results are reported in ‰ relative to VPDB. The overall reproducibility was better than 0.02‰ for $\delta^{13}C$ and 0.04‰ for $\delta^{18}O$. The values of $\delta^{13}C$ and $\delta^{18}O$ are in Table S1.

Previous data of texture, mineralogy and particularly the $\delta^{13}C$ and $\delta^{18}O$ values published by Arenas et al. (1997) are also considered in this work to support and complete the newly obtained results and the intervening stratigraphic portion between the newly sampled intervals (Figure 2). Section SAC provided a total of 54 samples (labelled Alc), 30 of which are located between the two intervals sampled anew in this study. A total of 19 samples were from section LAN (labelled L). All samples are identified in Table S1. Dolomite was not removed from the carbonate and marl samples prior to the isotopic analyses because of difficulties with this procedure (Sreenivasan et al., 2023; Yui & Gong, 2003). Instead, in order to know how much the Mg-bearing carbonates bias the isotopic composition of calcium carbonate (i.e. calcite), the obtained values of $\delta^{18}O$ for samples with dolomite and/or ankerite have been corrected based on the premise that the studied Mg-bearing samples are mostly primary precipitates (e.g. dolomicrite). These would have formed from the same parent water as calcite, either in the lake water or in the water pores very soon after calcite (Arenas et al., 1997) and linked to intense evaporation. Although dolomite always shows $\delta^{18}O$-enrichment with respect to calcite, there is no consensus about this difference in natural environments such as lakes. Uncertainties came from different sources (see references in Horita, 2014; Sreenivasan et al., 2023). Specifically, in natural environments, the $\delta^{18}O$ composition of dolomite can depend on a variety of parameters, like the stoichiometry and the degree of order/disorder of the dolomite or the presence of clay minerals (Bristow et al., 2012; Horita, 2014; Murray & Swart, 2017 and references therein).
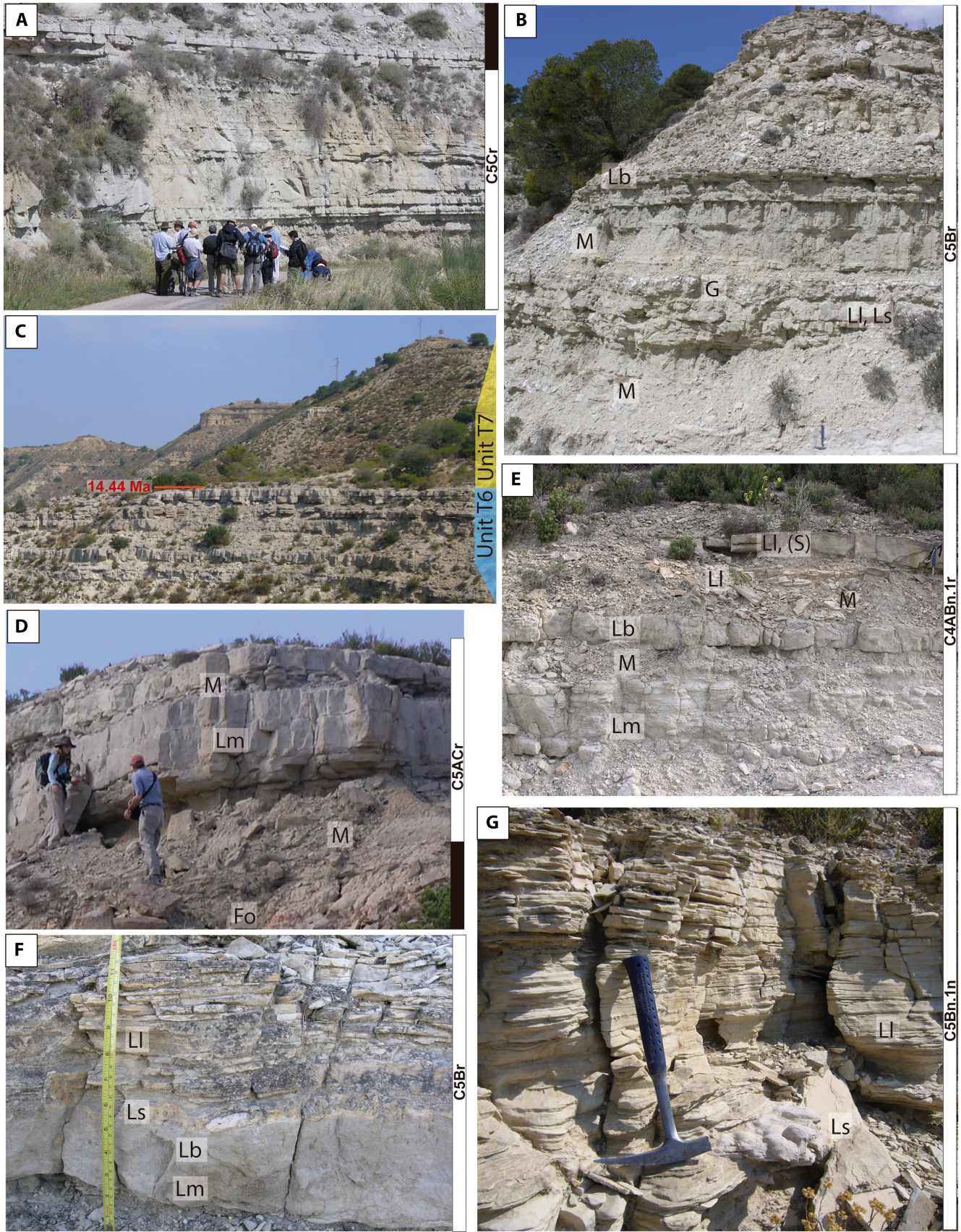
According to laboratory-based equations, the difference between $\delta^{18}O_{calcite}$ and $\delta^{18}O_{dolomite}$, at low temperature, can be as much as 3.6‰ (Murray & Swart, 2017),

although other authors give a narrower range (0.7–2.6‰; Horita, 2014). For natural dolomite in lakes, the correction ranges from 1 to 7‰ (Arenas et al., 1997; Valero-Garcés

FIGURE 3 Field views of the study area, with details of the Lanaja and San Caprasio sections. (A) Alternating limestones (facies Lm and Lb) and marls with interbedded sandstone lenses and mudstones (Lanaja). (B) Alternating marls and limestones (facies Ll, Ls, Lb) with interbedded gypsum nodules (facies G) (lower portion of San Caprasio). (C) Boundary between units T6 and T7 on the southern side of the Sierra de Alcubierre. Note the change from light grey tabular limestone strata in unit T6 to ochre mudstones and sandstone beds at the base of unit T7. (D) Thick tabular limestone strata (facies Lm) with interbedded marls (facies M). Note ochre mudstones (facies F) at the base of picture (upper portion of San Caprasio). (E) Alternating bioclastic limestones (facies Lm, Lb, Ll), locally sandstones and marls (facies M). Middle part of San Caprasio. (F) Detail of the abrupt contact between bioclastic limestones (facies Lm, Lb) and overlaying stromatolites (facies Ls) and laminated limestones (facies Ll). Although it is not visible in the image, the contact is erosive (lower half of San Caprasio). (G) Detail of stromatolite (Ls) at the base of a laminated limestone strata (facies Ll). San Caprasio, onset of the Perdiguera Member. Chrons indicated on the right side of images help location of images in Figure 7.

et al., 2000). In this paper, the $\delta^{18}O$ values of samples containing dolomite and/or ankerite have been corrected by a factor of 4‰ proportionate to the ratio dolomite + ankerite to calcite. This correction has been applied to samples having more than 10% dolomite + ankerite. It can be assumed that the resulting values are a rough estimate of the $\delta^{18}O$ values of the calcites that would have precipitated in equilibrium from the same parent water as dolomite (Arenas et al., 1997). No correction was applied to the $\delta^{13}C$ values, as the relationship between the dolomite + ankerite content and the $\delta^{13}C$ values is unclear and the $\delta^{13}C$ enrichment of Mg-mineral bearing samples is much lower than that of $\delta^{18}O$ (Arenas et al., 1997; Horita, 2014; Valero-Garcés et al., 2000).

3.5 | Magnetic susceptibility

The MS data available from Pérez Rivarés (2016) in sections LAN and SAC are used to complement the information regarding climate and depositional environment deduced from other proxies. The values were calculated from the same samples used to determine the magnetic polarity zones in sections LAN and SAC. For MS measures, the selected lithologies were grey marls and reddish, orange and light-brown mudstones. Limestones, sandstones and coarse-grained lithologies were avoided, so that the results would be more comparable. Lithology selection yielded an average sampling density of one site per 1–2 m. A total of 158 sampling sites from the marl and mudstones beds were analysed through the *ca* 289 m thick LAN and SAC sections (Table S3).

The MS measurements were conducted at the Palaeomagnetic Laboratories of the University of Barcelona (CCiTUB-CSIC) using a Kappabridge KLY-2 (Geofyzika Brno) susceptibility bridge. The bulk susceptibility was measured in 15 different directions on at least one sample per site, and a mean value was calculated. Volume normalised MS (κ) has been used as an estimate of the abundance of magnetic minerals and the values have been expressed in dimensionless International System units.

3.6 | Statistical treatment of data

For presentation purposes and inter data set comparisons, in order to reduce the data noise, the raw $\delta^{13}C$ and $\delta^{18}O$ values, including the already published data (Arenas et al., 1997), the calculated FWHM data from clay analysis and the raw MS mean values were smoothed using a local regression method (LOESS, Locally Estimated Scatterplot Smoothing) of the statistical program PAST software (Hammer et al., 2001; https://www.nhm.uio.no/english/research/resources/past/). The smoothing parameter used was 0.15. These procedures allow samples to be compared and trends to be deduced by reducing uncertainties and outliers.

4 | RESULTS

4.1 | Mineralogy

The mineralogical composition of bulk samples is shown in Table S2. Quartz, phyllosilicates and calcite are the main components. There are also significant amounts of dolomite and ankerite, mainly in section SAC. Carbonate minerals increase at the beginning of section LAN and decrease sharply at the end of section SAC, above the interval with high concentrations of dolomite and ankerite. Pyrite and haematite are more abundant at the end of section SAC. The mineralogical composition obtained through P-XRD analyses and optical microscope examinations of the newly studied samples along with that of the already studied samples yielded very consistent results, useful for palaeoclimate reconstruction (Table S2).

### 4.2 | Texture and post-sedimentary processes

The post-sedimentary features observed in hand samples and thin sections were micro-spar and spar calcite cements, which appear in intergranular and mouldic
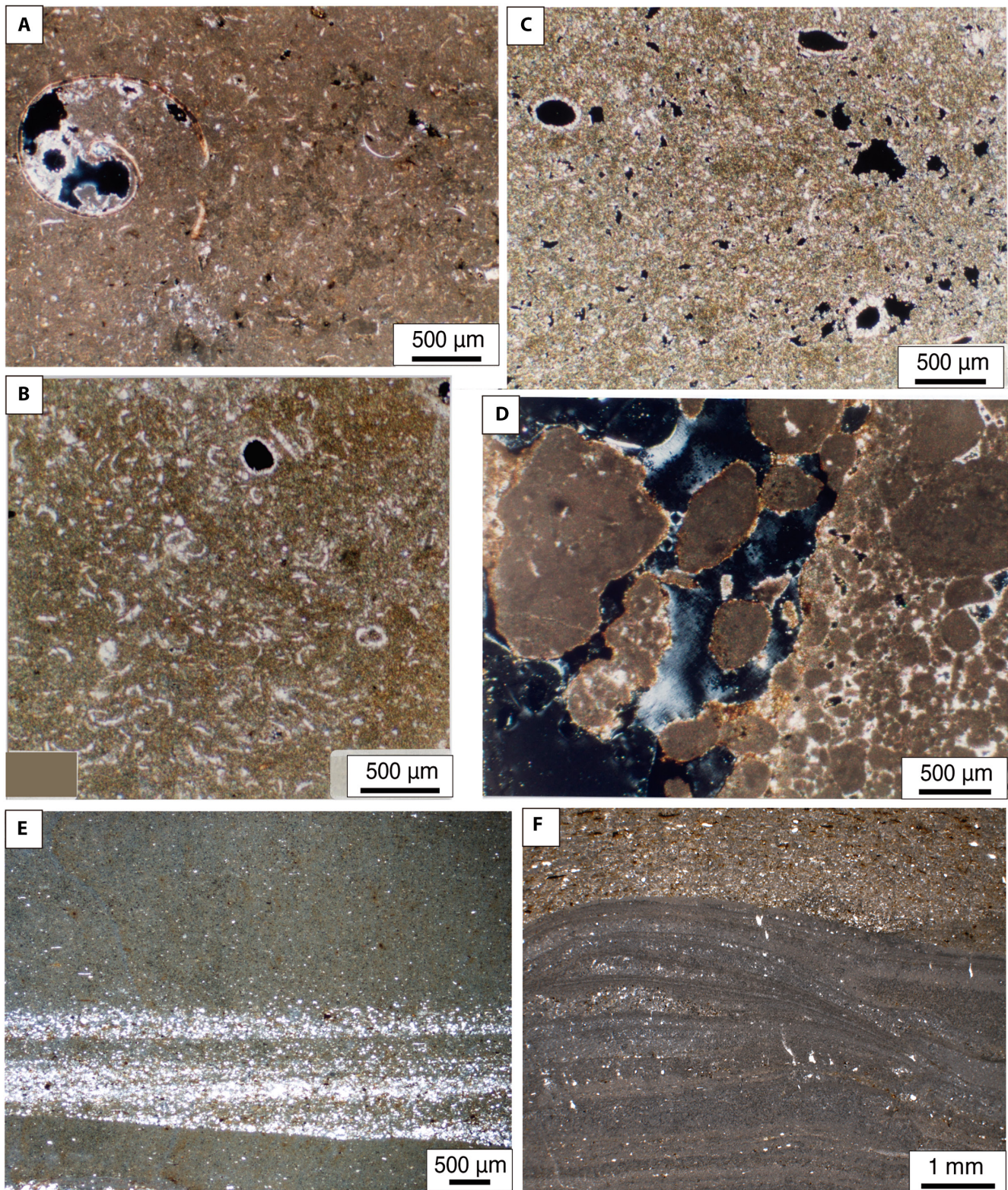
FIGURE 4 Photomicrographs of carbonate facies in the studied sections. Optical microscope with A–D using cross-polarised light. (A) Mudstone to wackestone containing gastropods, ostracods and charophyte fragments (facies Lm). (B) Wackestone with charophyte gyrogonites and charophyte fragments (facies Lm). (C) Wackestone with charophyte gyrogonites and charophyte fragments, and ostracods. Irregular cavities (black in colour) correspond to root traces (facies Lb). (D) Nodular limestone, resulting from bioturbation and desiccation (facies Lb). (E) Laminated limestone (facies Ll) formed of lime mudstone with interbedded silt-sized quartz grain laminae. Note the low-angle cross-lamination. (F) Slightly undulating laminae in stromatolite (facies Ls), topped by silt-sized carbonate and minor quartz grains of a laminated limestone (facies Ll). Laminae in Ls consist of light and dark micrite and microspar calcite, at places including thin intervals formed of silt-sized quartz grains.
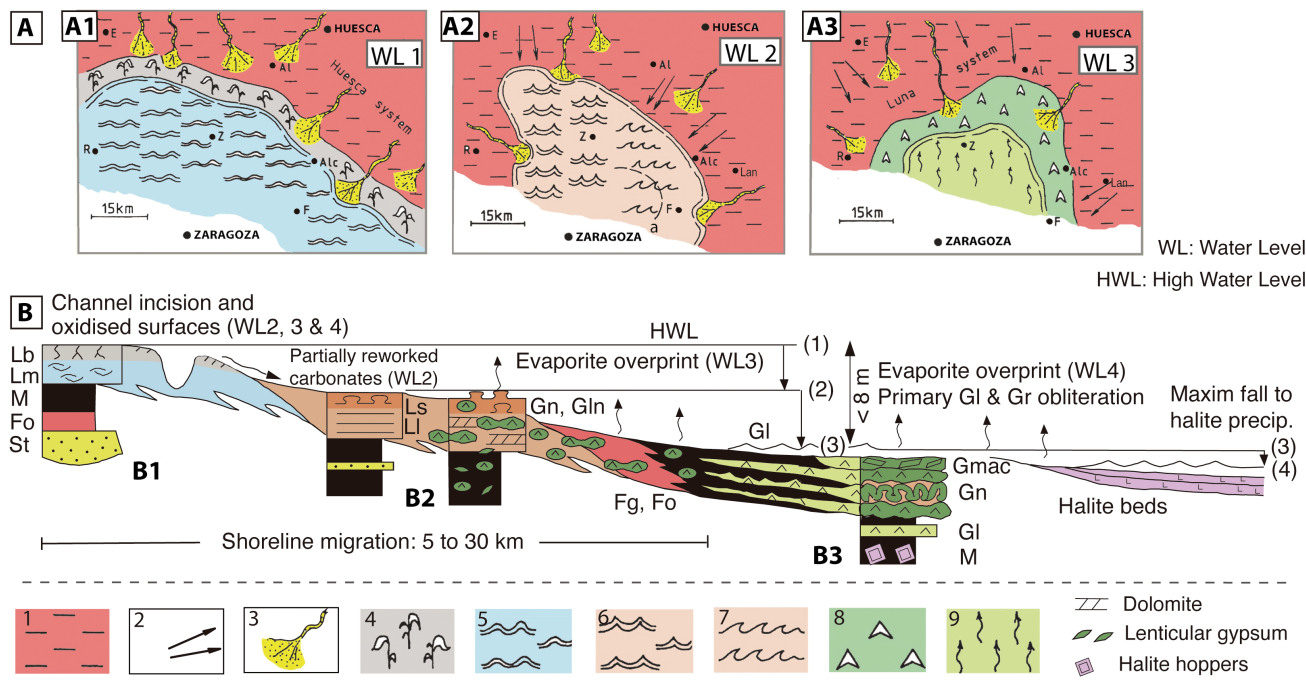
FIGURE 5 (A) Palaeogeographical schemes and (B) simplified sedimentary facies model for lacustrine systems of units T5, T6 and lower half of T7 in the central part of the Ebro Basin (Sierra de Alcubierre and Montes de Castejón). Modified from Arenas et al. (2007). Maps A1, A2 and A3 represent the distribution of depositional environments during certain time intervals corresponding to the upper part of unit T5 (A1: WL 1; A3: WL 3) and lower part of unit T6 (A2: WL 2); Line a in A2 indicates the approximate northern boundary of sulphate areas during WL 3. The model in B shows the different facies sequences and processes resulting from a continuous fall in lake water level from freshwater (HWL = WL 1) to saline carbonate (WL 2), sulphate (WL 3) and halite (WL 4) depositional environments. Sequence (B1): Distal alluvial to carbonate lacustrine expansion; sequence (B2): shallowing upward in saline carbonate environment; sequence (B3): shallowing upward in sulphate lacustrine environment and evaporite overprint. Legend for maps: 1: alluvial plain (distal sector of alluvial systems), with 2: sheet flows and 3: channelled flows; 4: palustrine margin; 5: freshwater carbonate depositional environments; 6: saline carbonate depositional environments; 7: surge-dominated area; 8: saline mud flat; 9: sulphate depositional environments. Localities: Alc Alcubierre, Al Almudévar, Lan Lanaja, E Ejea de los Caballeros, F Farlete, R Remolinos, Z Zuera. Legend for facies labels in Table 1.

TABLE 2 Average values of δ^{13}C and δ^{18}O (‰ VPDB) of samples analysed in the studied sections of the Sierra de Alcubierre.

Sections and samples	δ^{13}C (‰VPDB) Average ± s	δ^{18}O (‰VPDB) Average ± s	δ^{18}O(‰VPDB) (4‰)[a] Average ± s
LAN + L + SAC + Alc	−2.76 ± 1.12	−4.64 ± 2.17	−4.90 ± 1.52
N = 78 + 102 = 180			
LAN + L (N = 78)	−3.03 ± 0.90	−4.58 ± 1.74	−4.76 ± 1.28
Correl coef r		0.47	0.47
SAC + Alc (N = 102)	−2.92 ± 1.13	−4.60 ± 2.84	−5.00 ± 1.68
Correl coef r		0.47	0.57

Note: Correlation coefficient (r) between δ^{13}C and δ^{18}O. LAN and L: Lanaja section; SAC and Alc: San Caprasio section. LAN and SAC: data obtained in this work; L and Alc: data from Arenas (1993) published by Arenas et al. (1997). See Table S1 for individual values.

[a]δ^{18}O after correction of 4‰ of samples containing dolomite ± ankerite (see Section 3).

porosity. Dissolution and replacement features are not common. The studied carbonate samples consist of mudstones to wackestones, rarely packstones, containing diverse biota (facies Lm; Figure 4A,B). Root traces and calcite nodules and breccias are present in the bioturbated facies (facies Lb; Figure 4C,D). These features formed during or soon after deposition of lime mud as a result of lake water-level variation and plant activity, and

TABLE 3 Average values of δ^{13}C and δ^{18}O (‰ VPDB) of samples analysed in the studied sections of the Sierra de Alcubierre, grouped by sedimentary facies.

Section	Sedimentary facies	Number of samples	δ^{13}C (VPDB) ‰ Average ± s	δ^{18}O (VPDB) ‰ Average ± s	δ^{18}O (VPDB) ‰ Aver ± s (4‰)[a]	Correl coef r (1)	(2)
San Caprasio (SAN + Alc)	Ll	12	−2.52 ± 1.03	−4.87 ± 0.73	−4.87 ± 0.73		
	Ls	10	−2.62 ± 1.19	−4.44 ± 2.47	−4.82 ± 1.43		
	Ll + Ls	22	−2.57 ± 1.08	−4.68 ± 1.71	−4.85 ± 1.08	0.49	0.66
	Lm	11	−3.50 ± 0.76	−5.92 ± 0.80			
	Lb	5	−3.01 ± 1.22	−5.61 ± 0.82			
	Lm + Lb	16	−3.42 ± 0.90	−5.86 ± 0.81		0.47	
	M	14	−2.25 ± 0.95	−1.71 ± 3.68	−2.93 ± 2.09		
	F	21	−3.38 ± 1.16	−5.56 ± 2.28	−5.92 ± 1.91		
	M + F	35	−2.93 ± 1.20	−4.02 ± 3.71	−4.73 ± 2.45	0.67	0.75
Lanaja (LAN + L)	Ll	15	−2.34 ± 0.64	−3.43 ± 1.80	−3.94 ± 0.85		
	Ls	3	−2.40 ± 0.46	−3.87 ± 1.21	−4.35 ± 0.56		
	Ll + Ls	18	−2.35 ± 0.60	−3.50 ± 1.70	−4.04 ± 0.81	0.35	0.35
	Lm	9	−3.29 ± 1.30	−5.62 ± 1.61			
	Lb	14	−3.19 ± 1.24	−4.62 ± 1.49			
	Lm + Lb	23	−3.44 ± 1.09	−5.22 ± 1.17		0.44	
	M	15	−2.78 ± 0.57	−4.15 ± 2.42	−4.41 ± 1.69		
	F	19	−3.35 ± 0.70	−5.06 ± 1.28	−5.15 ± 1.12		
	M + F	34	−3.07 ± 0.70	−4.68 ± 1.87	−4.84 ± 1.41	0.39	0.35

Note: Correlation coefficient (r) between δ^{13}C and δ^{18}O: (1) using original δ^{18}O values; (2) using δ^{18}O values after 4‰ correction. Samples LAN and L: Lanaja section; Samples SAC and Alc: San Caprasio section. LAN and SAC: data obtained in this work; L and Alc: data from Arenas (1993) published by Arenas et al. (1997). See Table S1 for individual values. Shaded bands correspond to grouped facies.

Abbreviations: F, Siliciclastic fines (Mudstones); Lb, Bioturbated bioclastic limestones; Ll, Laminated limestones ± dolostones; Lm, Massive bioclastic limestones; Ls, Stromatolites limestones ± dolostones; M, Marls. marlstones (calcite ± dolomite ± ankerite).

[a]δ^{18}O after correction of 4‰ of samples containing dolomite ± ankerite (see Section 3).

thus, the textural features and isotopic composition of these facies are considered indicative of environmental parameters occurring in palustrine environments (Alonso-Zarza, 2003; Vázquez-Urbez et al., 2013). In the case of the laminated limestones, the detrital laminae that are interlayered within the dominant micrite or dolomicrite correspond to both carbonate and quartz grains (Figure 4E); scarce detrital content may also occur within some stromatolite laminae (Figure 4F). Some samples of facies Ll and Ls contain dolomite. There is no petrographic evidence of diagenesis within the dolomicrite samples. Dolomicrite is considered to have precipitated from the same parent water as calcite (i.e. without mixing of different water sources), very soon after calcite (see discussion in Arenas et al., 1997). Moreover, the large difference between calcite and dolomite δ^{18}O values supports a dominant non-diagenetic precipitation process, as suggested by Valero-Garcés et al. (2000). Based on these observations and the careful selection of samples for analyses, the isotopic values of the studied samples are considered suitable for providing depositional, climate and hydrological information.

4.3 | δ^{13}C and δ^{18}O composition

The δ^{13}C values of the analysed carbonate-bearing samples range from −6.4 to 0.09‰, with a mean value of −2.76‰ ± 1.12. The δ^{18}O values range from −9 to 3.66‰, with a mean value of −4.64‰ ± 2.17 (Table S1). However, average and correlation values vary depending on the sedimentary facies and also through time within the study sections (Tables 2 and 3; Figure S1).

4.3.1 | Stable isotopes and sedimentary facies

The δ^{13}C and δ^{18}O values of the different sedimentary facies define fields that partially overlap each other, with average values that set apart the different groups of facies (Figure 6A,B; Table S1), coinciding with previous results based on a smaller set of samples (Arenas, 1993; Arenas et al., 1997). Each facies and group of facies present consistent isotopic differences irrespective of the selected temporal interval and section (Tables 2 and 3). The stromatolitic and laminated facies (Ls and Ll), either
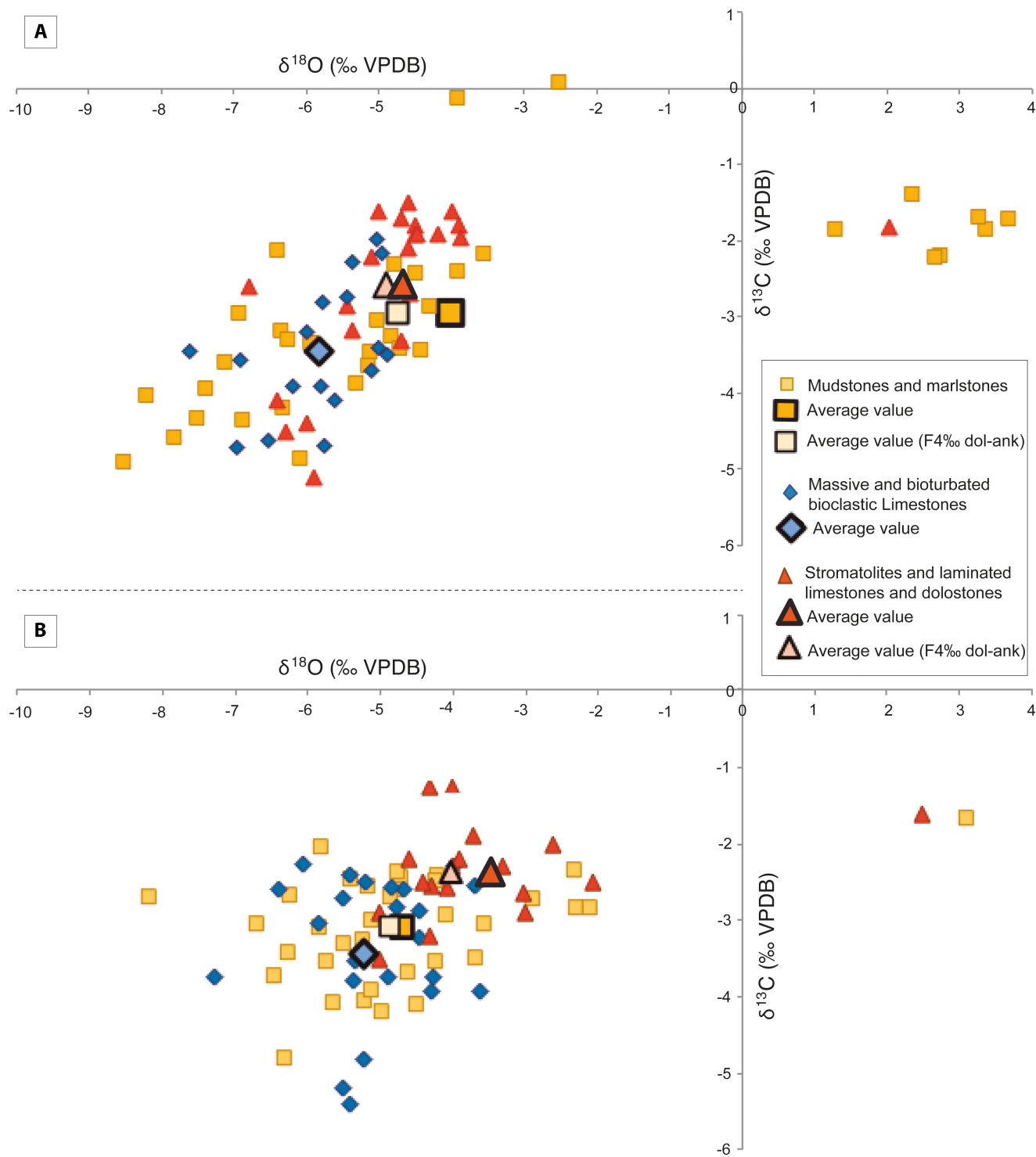
FIGURE 6 δ^{13}C versus δ^{18}O values (‰ VPDB) of all samples considered in this study (see Table S1 and Section 3 for details). (A) San Caprasio section. (B) Lanaja section. Samples with positive δ^{18}O values contain significant amounts of Mg carbonates.

limestones, dolomitic limestones or dolostones, present similar δ^{13}C and δ^{18}O values, having the highest average values of all samples. In this group, the highest δ^{18}O values, including those that are positive, are proportionate to the percentage of dolomite and ankerite in the samples. The massive and bioturbated bioclastic limestones (Lm

and Lb) have similar δ^{13}C and δ^{18}O values, although with slightly more negative average δ^{18}O values in the massive limestones than in the bioturbated. This group (Lm and Lb) presents the lowest average δ^{13}C and δ^{18}O values, while marls, marlstones and carbonate mudstones (M and F) have intermediate δ^{13}C and δ^{18}O values. In section

SAC, the δ^{18}O values of the Mg carbonate-bearing samples change the average δ^{18}O values towards higher values.

If the δ^{18}O values of Mg carbonate-bearing samples are corrected to calcite isotopic values (as explained in Section 3) and only calcite samples are considered, the average δ^{13}C and δ^{18}O values of the three facies groups are clearly separate in the two sections (Figure 6A,B; Table 3).

4.3.2 | Evolution of δ^{13}C and δ^{18}O values through time

The tendencies of the δ^{13}C and δ^{18}O values from single or grouped sedimentary facies (e.g. mudstones and marlstones, massive and bioturbated bioclastic limestones and laminated carbonate and stromatolitic facies) through time are similar to each other (Figure S1). Therefore, all the data can be used as single sets of values to infer the climate-related, depositional and hydrological processes of the studied succession. The LOESS smoothing of the δ^{13}C and δ^{18}O values series (as explained in Section 3) unveils several evolutionary trends (Figure 7). These smoothed trends are discussed below and compared with time series literature. Up to five main distinct trends can be distinguished in the evolution of δ^{13}C and δ^{18}O values through the LAN and SAC sections (Figure 7):

1. In the LAN section, both δ^{13}C and δ^{18}O values show generally increasing trends; most values of δ^{13}C are between −4 and −2‰ while δ^{18}O values have a much wider range of variability. Two intervals, designated segments a and b, are as follows:

   a. From the base of section (sample LAN-46) to 99–103 m (samples L-52b to L-59b), *ca* 17.73 to 17.10–17.06 Ma. This segment shows δ^{13}C values increasing from the base (sample LAN-46) to 66.8 m (peaking at sample L-101; 17.52 Ma), then decreasing to 99–103 m (samples L-52b to L-59b). The δ^{18}O values first delineate a gentle rise roughly coinciding with the peak δ^{13}C value at 66.8 m, then continue with an overall decrease to the end of segment.

   b. From the end of segment a to 169 m (sample LAN-204), corresponding to *ca* 16.31 Ma. A generally increasing trend in the δ^{13}C values extends throughout. The values of the upper half are less variable (mostly between −2 and −3‰; from 128 m, samples L-109 and LAN-162A, to the top) than those below. The δ^{18}O values also show an overall increasing trend. Several oscillations are depicted, with a latest maximum around 158 m. From this maximum to the top of this segment, there is a distinct shift to more negative values, with a narrower range of variability (−3.8 to −6‰) than seen below. This uppermost part spans from *ca* 16.43 to 16.31 Ma.

2. In the SAC section, overall decreasing trends are depicted by both δ^{13}C and δ^{18}O values, although the trend in δ^{18}O values is interrupted by a sharp increase in the second third. In detail, four segments, designated c, d, e and f, are as follows:

   c. From the base of the section (sample Alc-1a) to 133 m (samples SAC-141 and SAC-142), *ca* 16.12 to 14.86. The δ^{13}C values in interval c are highly variable (most being within 0 to −4‰). There is a gentle maximum close to the base, at 59.9 m (sample Alc-12), at 15.94 Ma, and a broad minimum at the end of segment c centred on sample SAC-134 (125 m; 14.97 Ma). The δ^{18}O values show a chiefly parallel evolution to those of δ^{13}C values, but with low δ^{18}O values extending up to the end of the segment.

   d. From the end of segment c to 153 m (sample SAC-159), corresponding to 14.56 Ma. The δ^{13}C values have a narrower range of variability (−2 to −1‰) with respect to segment c, the relative increase peaking at 147 m (sample SAC-155), at 14.62 Ma. The δ^{18}O values are in a clearly defined set with a sharp beginning and a sharp end, having extreme variability, from −5 and −7‰ to +1 and +3.6‰.

   e. From the end of segment d to 167 m (up to sample SAC-174A), corresponding to 14.41 Ma. An acute decrease is shown in the δ^{13}C values, evolving from *ca* −1.5 to −5‰. Likewise, the δ^{18}O values show an abrupt decrease, evolving from *ca* −4.5 to −8.5‰.

   f. From the end of segment e to 210.1 m (the last analysed sample: Alc-197c), corresponding to 14.0 Ma. Overall, the δ^{13}C values decrease, showing a wide range of variability (from 0 to −5, with most samples being between −2 and −5‰). In contrast, δ^{18}O values delineate a smooth increase through segment f, showing a wider range of variability (from −2.5 to −8.2, with most samples being between −4 and −7‰). From 193 m (sample SAC-191, *ca* 14.15 Ma) onwards, the trends in δ^{13}C and δ^{18}O values change from roughly parallel to opposing trends.

The calcite δ^{18}O values calculated from dolomite and/or ankerite-bearing samples (4‰ correction factor; see the Section 3) define the same increasing or decreasing trends as those without correction. In the case of segment c, the trend of the corrected δ^{18}O values is parallel to the δ^{13}C trend. In interval d, the calculated calcite values define a clear set, with less negative values, but still with sharp beginning and end.

4.4 | Illite crystallinity index (FWHM)

The FWHM values range from 0.105 to 0.354 in the LAN section (x=0.167); in the SAC section, they are slightly lower, ranging from 0.100 to 0.247 (x=0.145). The variability is also lower at SAC (s=0.039 at SAC and s=0.052 at LAN). Roughly, FWHM values seem to increase through the section at LAN, while they decrease through the section at SAC (Figure 8C). Like the evolution in stable isotope values, the smoothed crystallinity index line allows several intervals to be distinguished through time. However, it should be taken into account that this evolution corresponds to fewer data points than the isotopic trends, with a long gap between the LAN and SAC sections that spans 16.3–15.1 Ma. Three intervals have been identified (Figure 8C):

1. From 17.7 to 17.1 Ma (segment a), the FWHM values oscillate below *ca* 0.15.
2. From 17.1 to 16.3 Ma (segment b), there is a gentle increase, peaking at the maximum value of 0.21, at *ca* 16.9 Ma.
3. From 15.1 to 14.0 Ma, the trend decreases, first more steeply to *ca* 14.9 Ma, then more gently. At 14.3 Ma there is a turning point, with a minimum value of 0.111, then gently rising up to 13.9 Ma (upper part of segment f).

4.5 | MS data

MS curves show variations due to changes in the concentration of fine-grained magnetic minerals (Figure 8D). The sharpest change occurs between 14.6 and 14.4 Ma (SAC section), with a significant increase concurrent with a decrease in FWHM values (Figure 8C). The lowest MS values coincide with the highest $\delta^{18}O$ values and a $\delta^{13}C$ maximum around *ca* 14.62 Ma (Figure 8A,B).

5 | DISCUSSION

In closed-lake systems dominated by chemical precipitation, as in this case, the lake-level variations are related to water input, either groundwater or surface supply, and evaporation, primarily dependent on climate conditions (Alonso-Zarza et al., 2012; Gierlowski-Kordesch, 2010; Kelts & Talbot, 1990; Valero-Garcés et al., 2000). These variations are reflected by changes in mineralogy, sedimentological features and geochemical composition of the sediments, either as single sedimentary facies or as facies associations over different timescales. Likewise, the spatial distribution of lithofacies belts through time can also reflect such lake level changes (Figure 5A; Arenas & Pardo, 1999; Platt, 1989).

The evolution of the illite crystallinity index and MS of distal alluvial, lacustrine and palustrine sediments through time are often used to estimate rates of climate-associated chemical and/or physical processes within the watershed and are transferred to lake systems (Bastida et al., 2017; Mandic et al.; 2011; Song et al., 2018). Illite is an inherited mineral within the fine detrital deposits of alluvial and lake systems. Since the illite crystallinity index depends on the intensity of sediment hydrolysis, it represents the intensity of chemical alteration (weathering) in the source area. The larger the index, the more intense the chemical alteration undergone by these sediments. In terms of climate parameters, the illite crystallinity index reflects a warmer and/or humid scenario in the source area.

The oxygen isotopic composition of lake water depends on (1) the isotopic composition of the rainfall, its temperature and amount, (2) humidity and evaporation and (3) groundwater inflow (Deocampo, 2010; Leng & Marshall, 2004; Talbot, 1990; Valero-Garcés et al., 2000). In closed lake systems, the effects of evaporative processes on the lake water composition can be intense and also on the interstitial water in the exposed areas surrounding the lake. Changes in the precipitation/evaporation ratio (P/E) produce effects on the $\delta^{18}O$ composition of lake and interstitial water that are opposite to those caused by temperature changes. Thus, the evolution of $\delta^{18}O$ values of the resulting deposits cannot be interpreted as a function of a single parameter. If no major changes in the water sources are produced, a decrease in $\delta^{18}O$ values of the deposits can be interpreted in terms of increasing P/E or hydrological balance or lake water renewal (due to increased inputs of isotopically lighter water) and decreasing air temperature (as cool precipitation is isotopically lighter than warm precipitation). The effects of temperature on $\delta^{18}O$ fractionation during carbonate mineral precipitation are considered of secondary importance with respect to the temperature effects on the $\delta^{18}O$ values of the meteoric water (Deocampo, 2010; Dworkin et al., 2005).

In the case of the carbon isotopic composition, the dissolved inorganic carbon in the lake water depends on (1) the source rock composition; (2) the biological activity in and around the lake and watershed, including soil development, and thus the ^{12}C contribution to the lake system; (3) photosynthesis in the lake water; and (4) the atmospheric-CO_2 equilibration with dissolved carbonate species in the lake water (Leng & Marshall, 2004; Talbot & Kelts, 1990). Assuming the $\delta^{13}C$ source rock and groundwater composition of the lake did not change through time, a decrease in $\delta^{13}C$ values of the deposits can be interpreted in terms of increasing humidity, with rising plant and soil development.
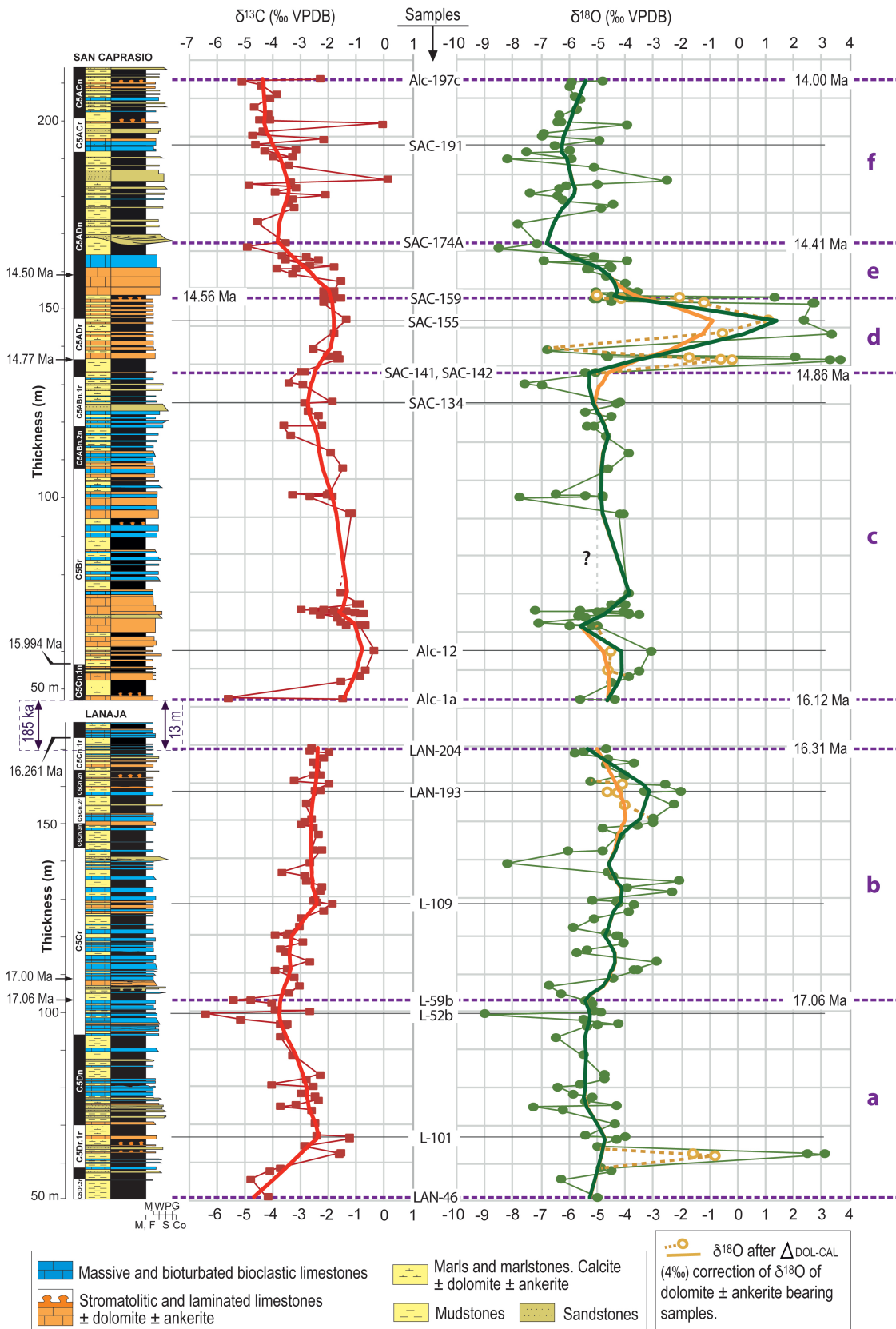
FIGURE 7 Stratigraphic sections (Lanaja and San Caprasio) with location of samples and their $\delta^{13}C$ and $\delta^{18}O$ composition. The diverse segments (a–f) correspond to smoothed tendencies and are described in the main text. Some ages and sample labels are indicated for guiding. Smoothed curves have been calculated by LOESS method (locally estimated scatterplot smoothing). For geomagnetic polarity (Ogg, 2020), see Figure 2.
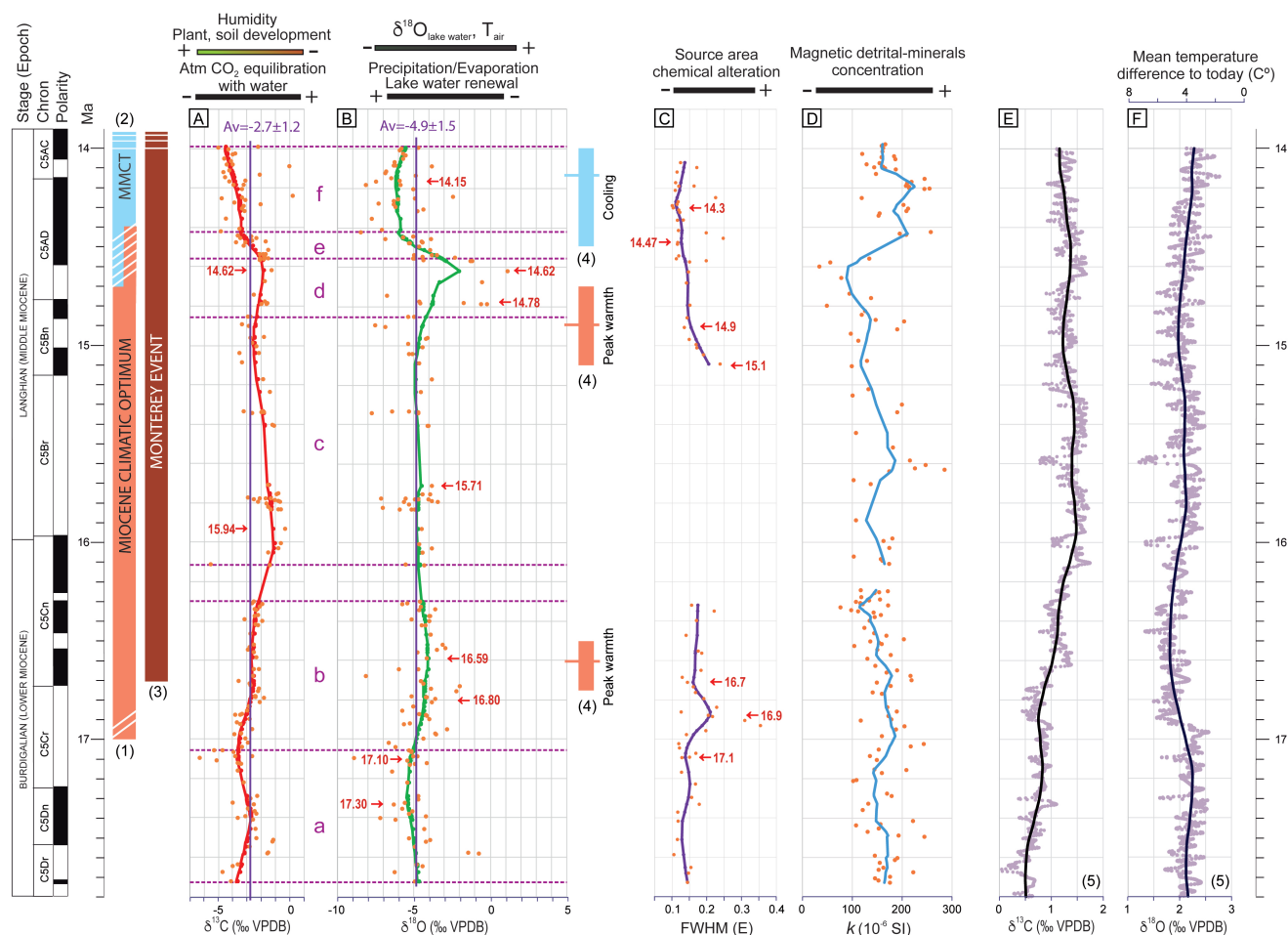
FIGURE 8 Comparison between (A) $\delta^{13}C$ and (B) $\delta^{18}O$ isotope records (this work), (C) variations of FWHM of 001 reflection (*ca* 10 Å) from clay fractions (this work); (D) *k*, volume normalised magnetic susceptibility (Pérez Rivarés, 2016) from Lanaja and San Caprasio sections; (E) and (F) Cenozoic global reference benthic foraminifer carbon and oxygen isotope dataset (CENOGRID) from ocean drilling core sites spanning 17.8–14 Ma. Smoothed curves in A, B, C and D have been calculated by LOESS method (locally estimated scatterplot smoothing); $\delta^{18}O$ values are those after 4‰ correction for dolomite and/or ankerite. Absolute ages for epochs, stages and geomagnetic polarity from Ogg (2020). (1) Holbourn et al. (2015), Steinthorsdottir et al. (2020), Westerhold et al. (2020): 17-16.9 to 14.7-14.6 Ma; (2) Holbourn et al. (2015): 14.7 to 13.8 Ma; (3) Holbourn et al. (2007, 2015); (4) Methner et al. (2020); (5) Westerhold et al. (2020). Oblique white lines on light red (1) and blue (2) vertical bands represent the main range of ages proposed by different authors for the beginning and end of MCO and the beginning of MMCT.

5.1 │ Mineralogical, sedimentological and $\delta^{13}C$ and $\delta^{18}O$ composition of the sedimentary facies: sedimentary context, hydrology and climate

The newly obtained mineralogical, textural and $\delta^{13}C$ and $\delta^{18}O$ results are consistent with previous studies of the same area (Arenas et al., 1993, 1997; Arenas & Pardo, 1999) which indicated that the several sedimentary facies formed as a result of distinct depositional, climate and hydrological conditions, that is, primarily those defined by sediment supply, water input (precipitation versus evaporation) and hydrodynamics. Likewise, these authors concluded that the isotopic compositions of the facies and their variations through time were related to

the depositional sedimentary conditions, which depended on climate variations over different timescales.

In brief, mineralogical, sedimentological and $\delta^{13}C$ and $\delta^{18}O$ results (Figure 6 and Figure S1; Tables 1 and 3) suggest that massive and bioturbated bioclastic limestones (with the lowest $\delta^{13}C$ and $\delta^{18}O$ values) formed in freshwater (calcium bicarbonate water) with diverse and abundant fauna and flora. These facies developed on low slope lake margins, including palustrine fringes, at times of high lake water levels (Figure 5A1,B1), during periods of considerable water input, likely coinciding with wet conditions (cf. Arenas & Pardo, 1999; Platt, 1989). Laminated and stromatolitic facies (with the highest $\delta^{13}C$ and $\delta^{18}O$ values) represent saline, calcium-bicarbonate-rich water in which microbial mats developed and wave activity formed a variety of structures

(Martín-Bello et al., 2019a, 2019b). These two facies were associated with lower lake water levels, during periods of less abundant water input, likely coinciding with arid or less humid conditions (Figure 5A2,B2). Dolomite and ankerite could precipitate in such conditions, from lake and interstitial water, directly from the lake water and pene-contemporaneous to calcite (Arenas et al., 1997; Casado et al., 2014; Pavelić et al., 2022). Marls, marlstones and carbonate mudstones (with intermediate $\delta^{13}C$ and $\delta^{18}O$ values) are associated with periods of surface water supply to the lake. Deposition took place in sublittoral and offshore areas. In arid conditions, lowering lake levels would cause such marly areas to become saline mud flats in which Mg-carbonate and Ca-Mg sulphate minerals could form interstitially (Figure 5A3). Calcium sulphate and halite facies formed in salinas and in saline mud flats (Figure 5A3,B3; Salvany, 1997). These evaporative facies reflect the lowest lake water levels and were associated with very arid phases. Siliciclastic mudstones and sandstones interbedded through the studied sections represent distal alluvial sediments, which deposited on the alluvial plains and also entered the lake. Other studies on lake systems have suggested similar sedimentological interpretations of the carbonate and sulphate lacustrine deposits (Gierlowski-Kordesch, 2010; Graf et al., 2015; Pavelić et al., 2022; Rhodes & Carroll, 2015).

Regarding the composition of the three groups of carbonate facies in the LAN and SAC sections (Figure 6, Table 3), in the case of $\delta^{13}C$, the average values of the three groups of facies are very similar in the two sections; only a small difference concerns facies Ll and Ls, which are on average ca 0.3‰ more negative in SAC than in LAN, likely suggesting overall slightly higher humidity and soil-derived CO_2 input in the SAC section. The average $\delta^{18}O$ values of facies groups Lm + Lb and Ll + Ls are lower in the SAC section than at LAN (regardless of mineralogy), indicating overall higher P/E after ca 16.1 Ma. Carbonate mudstones, marls and marlstones have similar average $\delta^{18}O$ values in both sections, but the large dispersion precludes stating clear differences through time. The aforementioned differences based on the isotopic composition of all the facies through time are consistent with those described by Arenas et al. (1997) considering units T5, T6 and T7 as temporal units for comparison.

5.2 | Evolutionary trends of $\delta^{13}C$ and $\delta^{18}O$ values, illite crystallinity index and MS through time in the Ebro Basin

5.2.1 | $\delta^{13}C$ and $\delta^{18}O$ values

For evolutionary and correlation purposes, the $\delta^{13}C$ and $\delta^{18}O$ values of the two studied sections have been reunited and treated as single sets of data representing time series, using the same LOESS smoothing conditions as in the case of Figure 7 (Figure 8A,B). In these series, the $\delta^{18}O$ values of Mg-bearing carbonate samples are those corrected by 4‰, as explained in the Section 3. The interval from 16.2 to 15.4 Ma has a lower sampling frequency compared to the intervals below and above. There is a short gap between the two sections (ca 185 ka) and a longer gap (ca 300 ka) devoid of isotopic data within the SAC section. Nonetheless, the available data add information on the climate and depositional conditions in the interim between the beginning and ending of the MCO.

The evolution of $\delta^{13}C$ and $\delta^{18}O$ values through time shows several distinctive trends that do not always run parallel to one another or are not fully synchronous (Figure 8A,B). Several intervals and trends can be seen on different scales.

Regarding the $\delta^{13}C$ smoothed line, on a broad scale and using as a central reference value the $\delta^{13}C$ average from all samples (-2.7 ± 1.2‰), three clear intervals can be distinguished (Figure 8A). The first interval spans from 17.7 to ca 16.8 Ma. Most values are lower than the average, having an increasing–decreasing–increasing evolution, with the minimum at ca 17.10 Ma. The second interval spans from ca 16.8 to 14.5 Ma, with most values higher than the average, and two maxima at ca 16 Ma and 14.6 Ma. The third interval spans from ca 14.5 to 13.9 Ma and has most values below the average, depicting a clear decreasing trend. These values represent the lowest $\delta^{13}C$ values throughout the section. Within these three broad intervals, some peaks or evolutionary tendencies mark several smaller $\delta^{13}C$ trends. Some of these smaller trends broadly coincide with those obtained using thickness data (Figure 7). Together, in terms of varying humidity, and the associated biota and soil development, the $\delta^{13}C$ variations in the studied sections represent (Figure 8A):

1. An initially oscillating variation, with a minimum around 17.4 Ma, a maximum between 17.10 and 17.06 Ma, and then a drop until ca 16.8 Ma, coinciding with segment a and part of segment b.
2. Since 16.8 to ca 16.5 Ma, more or less stable humidity conditions occurred, with the $\delta^{13}C$ line coinciding with the average value, covering a long part of segment b.
3. After this steady situation, humidity first decreased up to ca 16 Ma and then gradually rose up to 15–14.9 Ma, that is, most part of segment c.
4. A fall to a relative minimum in humidity is recorded at ca 14.6 Ma, parallel to the end of segment c and most of segment d.
5. From 14.6 to 13.99 Ma humidity increased; first sharply up to ca 14.41 Ma (segment e)—reaching $\delta^{13}C$ values

similar to those at 17.1 Ma—and then more gradually up to a maximum humidity at 13.99 Ma (segment f).

The latter situation (segment f) agrees with large water and sediment supply to the lake basin. The opposite context, poor lake water renewal during arid periods, would favour atmospheric-CO_2 equilibration with the carbonate species in the lake water, leading to higher $\delta^{13}C$ calcite values (e.g. relative maximum within segment a, beginning of segment c and most segment d). In this respect, the isotopic increases within the poorly sampled interval might have been exaggerated by local effects related to the offshore position of the SAC section, in which the lake water would experience high atmospheric-CO_2 equilibration and evaporation effects during periods of low lake water level. Maximum $\delta^{13}C$ values are recorded in an interval dominated by laminated and stromatolitic facies (Ll and Ls) at the beginning of the SAC section (base of segment c in Figure 7). These facies formed during periods of lowered lake level due to reduced water supply and high evaporation, resulting in saline carbonate lake water (Figure 5A2,B2).

The $\delta^{18}O$ smoothed line also delineates distinct intervals with respect to the average $\delta^{18}O$ value ($-4.9 \pm 1.5‰$) from all samples (Figure 8B). These intervals are almost coincident with those distinguished based on thickness data in Figure 7. The changes indicated by the $\delta^{18}O$ smoothed line can be interpreted as a function of (i) the P/E and the associated lake water level variations or changing lake water renewal, and (ii) the air temperature (T_{air}), which influences the evaporation rate and, above all, the rainfall $\delta^{18}O$ composition and thus the $\delta^{18}O$ composition of the lake water (Figure 8B). Following these ideas, the studied sections record:

1. An increase in P/E from 17.73 Ma up to approximately 17.30 Ma, that is, the lowest values of segment a.
2. This is followed by a slow drop in P/E, reaching a peak at *ca* 16.6 Ma, that is, the highest values of segment b.
3. Mostly stable conditions seem to have characterised a long period between 16.1 and 15 Ma (most of segment c). This long stable period includes the poorly sampled interval; thus, other variations, if any existed, might not be recorded by the $\delta^{18}O$ smoothed line.
4. A rise of evaporation (low P/E) is inferred from the sharp increase in $\delta^{18}O$ values, starting at *ca* 14.9 Ma and reaching a maximum at 14.62 Ma (within segment d); whether it is associated with an increase in T_{air} is unclear. These conditions could favour the precipitation of dolomite and ankerite, as recorded by the marl deposits that yielded the highest $\delta^{18}O$ values. Likewise, some marls, marlstones and limestones in this interval reflect the effects of shallowing and evaporative

processes through the presence of nodular gypsum, both scattered and forming beds. This isotopically heavy interval partly coincides with an evaporite-rich depositional wedge, that is, the Perdiguera Member (Arenas, 1993; Arenas & Pardo, 1999). Nonetheless, the intense effects of high evaporation could have obliterated the opposite effects of an initial cooling on the $\delta^{18}O$ composition of the lake water.

5. After that evaporation peak, a sharp rise in P/E is represented by a drop in $\delta^{18}O$ values from 14.56 to 14.41 Ma (segment e), followed by a gentle increase in P/E up to 14.15 Ma; from this time a slight decrease in P/E is recorded up to 13.99 Ma (segment f).

The overall increase of the P/E after 14.56 Ma favoured the following: (i) the final phases of lake expansion, as recorded by the abundance of massive and bioturbated bioclastic limestones up to 14.44 Ma (i.e. the boundary between units T6 and T7), (ii) the growth of vegetation and (iii) the development of the fluvial system, that is, the Huesca system, providing freshwater to the lake. Distal fluvial deposits are interbedded with the dominant-freshwater lacustrine deposits in this younger part of the section (i.e. belonging to unit T7). The rise in P/E may have coincided with T_{air} diminishing, which would have slowed down the chemical alteration in the catchment area.

5.2.2 | Illite crystallinity index (FWHM)

Given that illite in the studied lacustrine and distal alluvial sediments is an inherited mineral (Bauluz Lázaro et al., 1994), the oscillations defined by FWHM (Figure 8C) can be interpreted in terms of variations in the degree of chemical alteration in the sediment source area (Mesozoic and Cenozoic detrital rocks and carbonate rocks of the Pyrenean Central Unit and Palaeozoic formations of the Pyrenean Axial Zone). Low values are recorded from 17.7 until 17.1 Ma (segment a), then the chemical alteration strongly increases, reaching a maximum at 16.9 Ma, and then decreases until 16.7 Ma (within segment c). From 15.1 Ma onwards, the chemical alteration decreases, first rapidly until 14.9 Ma, then slowing down, with a gentle rise at the end of the record. In general, chemical alteration increases in the section at LAN and decreases at SAC.

The increase in P/E inferred from the stable isotope composition of the studied deposits since 14.56 Ma onwards mostly coincides with low FWHM values, which indicates low chemical alteration (Figure 8C) and is consistent with low T_{air}. Therefore, in the study area, diminishing T_{air} accompanied the increasing P/E from 14.56 Ma to the end of the studied section (13.99 Ma).

5.2.3 | Magnetic susceptibility

Lake sediments with higher concentrations of terrigenous material are generally characterised by a higher concentration of magnetic minerals (Geiss et al., 2003), so MS studies can characterise changes in detrital inputs that may reflect environmental responses to changes in climate. However, variations in detrital inputs into the lake basin could also be linked to changes in the relief of the sediment source area caused by tectonics. Increases and decreases in MS values of the predominantly lacustrine intervals through the two studied sections would be indicative of variations in the input of detrital material during changes in lake level. The MS minimum values are in segment d, fitting relative arid and warm conditions, as suggested by the highest $\delta^{18}O$ values and the relative $\delta^{13}C$ maximum at around 14.62 Ma (Figure 8A,B). However, the large increase in MS values above 14.5 Ma (Figure 8D) coincides with a significant increase in the supply of detrital material into the basin (Figure 2), concurring with the dominantly humid and cold conditions indicated by the $\delta^{13}C$ and $\delta^{18}O$ values, and with the low chemical alteration inferred from the FWHM variations in the same time interval (Figure 8A through D). These results support the idea that the large supply of detrital material into the basin after 14.44 Ma reflects a tectonic process in the catchment area during a period of change to humid and cold conditions. Subsequently, the carbonate lake system experienced a southward shift.

5.2.4 | Summary of principal features of the MCO and the MMCT

The aforementioned findings allow the beginning and end of the MCO in the Ebro Basin to be characterised as follows:

The onset of the MCO: It is characterised by a rise in humidity until 17.1–17.06 Ma, which then progressively diminishes until *ca* 16 Ma. A gradual increase of T_{air} occurs from 17.3 until *ca* 16.6 Ma. There is a gradual increase in chemical alteration with a peak at 16.9 Ma. An overall decrease, with short oscillations, in the concentration of magnetic detrital minerals is recorded until *ca* 16.2 Ma, peaking at *ca* 17 Ma.

The end of the MCO and the beginning of the MMCT: A gradual fall in humidity and P/E occurs from 14.9 until 14.6 Ma. After 14.56 Ma, there is an abrupt increase in P/E and cooling, which continued more gradually from 14.41 until 13.99 Ma, with a cooling peak at 14.15 Ma. A slight cooling of T_{air} might have begun earlier, by 14.6 Ma, but the concurrent intense evaporation (low P/E) could have masked its effect on the bulk $\delta^{18}O$ values of the lake water. A gradual

falling of chemical alteration is detected up to 14.3 Ma. A decrease followed by a sharp increase in the concentration of magnetic detrital minerals are parallel to P/E evolution.

5.3 | Comparison with other records

The results obtained in this study, spanning from 17.7 to 13.9 Ma, fully covering the MCO and including the MMCT, agree with those from other studies in nearby areas of the Ebro Basin based on sedimentology, palaeontology and low-resolution sampling of the $\delta^{13}C$ and $\delta^{18}O$ composition of distal alluvial and lacustrine deposits (Larena et al., 2020; Suarez-Hernando, 2017; Vázquez-Urbez et al., 2013). Collectively, these results are consistent with the changes in temperature and humidity reported for the Burdigalian-Langhian in other continental (Calvo et al., 1993; Methner et al., 2020; Pavelić et al., 2022; Trayler et al. 2020; Vázquez-Urbez et al., 2013) and marine examples (Holbourn et al., 2018; Steinthorsdottir et al., 2020; Westerhold et al., 2020). However, the degree of coincidence varies depending on the studies.

With respect to the illite crystallinity index, the entire MCO has been studied in marine sediments accessed by two drill cores in the South China Sea. In one case, spanning from 23 to 11 Ma, He et al. (2022) obtained illite crystallinity index values that ranged from 0.14 to 0.21, rising distinctly at 16.2 Ma. This result was interpreted to reflect the enhanced warm and humid conditions of the MCO. Values then decreased rapidly from 14.4 to 13.8 Ma, interpreted by the authors as the interval experiencing the dry, cold climates of the MMCT. At another site, from 17.17 to 12.69 Ma, Ma et al. (2023) calculated illite crystallinity index values ranging from 0.16 to 0.21. The values increased just after 17 Ma (i.e. at the MCO onset), then decreased after 14.7 Ma, and at the end of this interval, *ca* 14.2 Ma (MMCT), they became steadier. According to the boundaries established in the literature, those results were also indicative of more humid conditions during the MCO and a drier climate during the MMCT. The higher variability of the illite crystallinity index during the MMCT was interpreted to represent enhanced seasonality.

There are not many studies using illite crystallinity in continental materials of the MCO. The high illite crystallinity index during the MCO has been linked to warmer and more humid conditions in continental sediments in Asia (Song et al., 2018). In the study of a red clay succession from 17 to 12 Ma in north-west China, the illite crystallinity index is >0.4, with the highest values corresponding to the interval dated between 16 and 14 Ma, which permits the authors to interpret this interval as the MCO. Conversely, illite crystallinity index values are lower in the pre-MCO and post-MCO intervals (Song et al., 2018).

As in the study case in the Ebro Basin, the relationship between high MS values and high humidity has also been recorded in other studies on soils and lake sediments (Maher et al., 2003; Mandic et al., 2011). Although the strength of this parameter as a climate indicator usually relies on support from other proxies, in this study, it suits well the evolution of P/E and the chemical alteration rate in the source area.

Regarding the marine record, there are a number of studies using different proxies, but the $\delta^{13}C$ and $\delta^{18}O$ composition of benthic foraminifera has proved particularly valuable. Compilations of high-resolution $\delta^{18}O$ and $\delta^{13}C$ records from benthic foraminifera (Steinthorsdottir et al., 2020; Westerhold et al., 2020) indicate temperature and ^{12}C-related variations that are in accordance with the results obtained in the studied lake system of the Ebro Basin (Figure 8A,B,E,F) for both varying characters or parameters and timing.

Collectively, the variations in temperature and ^{12}C-contribution to the sedimentary system in the marine record match some of the general changes inferred for the lacustrine case studied herein. For example, the interval from *ca* 17.1 to 16.3 Ma approximately suits the temperature increase reported from the marine record (Figure 8F; Westerhold et al., 2020), but with a delay in the marine record (Figure 8F). The interval of maximum temperature values in the marine record is reported between 16.6 and 16.4 Ma (Figure 8F), partially coinciding with the interval of maximum temperature in the study area, but peaking approximately 100 ka earlier in the lacustrine record (Figure 8B,F).

One peculiarity of the MCO is the positive shift in $\delta^{13}C$ values, known as the Monterey excursion (Vincent & Berger, 1985), which lasted from 16.9 to about 13.5 Ma (Holbourn et al., 2007), and has been recorded in foraminifera from open waters, but also in shallow water settings of Central Europe, in the Apennines (Brandano et al., 2017). The interpretation of this event is complex, including orbital cycles as a driven factor (Holbourn et al., 2007). In the case of the studied continental record, the evolution in $\delta^{13}C$ values from 16.5 to 14.5 Ma (Figure 8A) delineates a positive shift which may correspond to the Monterey excursion. Several maxima have been described through this event (Holbourn et al., 2007; Woodruff & Savin, 1991), but these cannot be recognised in the studied record. However, the most outstanding maximum of this interval, about 16 Ma in the study area, may be the counterpart of the concurrent maxima recorded in the Apennines record (Brandano et al., 2017), specifically the CM3 of Holbourn et al. (2007).

In accordance with global climate tendencies inferred from marine cores, many terrestrial biota records reflect warm and humid conditions during the Early and Middle Miocene. However, this is not always the case (Steinthorsdottir et al., 2020). Trayler et al. (2020), using $\delta^{13}C$ and $\delta^{18}O$ values from the tooth enamel of fossil herbivores in distal fluvial and floodplain deposits in Patagonia, estimated a temperature increase between 16.9 and 16.4 Ma, which suits well the temperature rise reported from the marine record (Figure 8F; Westerhold et al., 2020) and also parallels the increase in $\delta^{18}O$ values between 17 and 16.3 Ma in the studied deposits of the Ebro Basin (Figure 8B). However, the aridification estimated by Trayler et al. (2020), based on $\delta^{13}C$ values, from 17.4 to 16.9 Ma is not recognised in the studied deposits of the Ebro Basin. This issue can be related to multiple causes, including the different altitude and latitude, and highlights the regional character of the hydrological response to climate changes. Moreover, another study based on microvertebrate assemblages of distal alluvial and lacustrine deposits of the Ebro Basin (Suarez-Hernando, 2017) reported the establishment of warm conditions at 19 Ma, *ca* 2 Ma before warming was detected in the marine record; the thermal maximum was detected at 17.4 Ma. Younger rodent assemblages also indicated warm conditions and a significant increase in humidity following lake expansion (Larena et al., 2020). These cases exemplify the regional heterogeneity in terrestrial ecosystem response to MCO conditions (Harris et al., 2020).

Additional valuable data regarding precipitation and temperature can be estimated from soil types, weathering ratios and the chemical index of alteration (Hamer et al., 2007) and, in carbonate-bearing soils, from $\delta^{13}C$ and $\delta^{18}O$ values and carbonate clumped isotopes. Methner et al. (2020) provided clumped isotope temperatures ($\Delta47$) from carbonate palaeosols formed in floodplain alluvial deposits in Central Europe (molasse basin, Switzerland) covering the interval 18–14 Ma. These authors reported two temperature ($\Delta47$) maxima for soil water: one at 16.6 Ma and another between 15.4 and 14.5, peaking at 14.9 Ma (Figure 8). The first warm maximum fits well the increase in $\delta^{18}O$ values between 16.7 and 16.5 Ma, peaking at 16.6 Ma, recorded by the studied lake deposits. The second warm maximum might correspond, in the study area, to the second increase in $\delta^{18}O$ values, which spans from 14.85 to 14.56 Ma, with a peak at 14.62 Ma, and therefore it would be delayed in the study lake record. It is worth noting that these authors also detected a remarkable temperature change after 14.5 Ma, reaching a minimum at 14.1 Ma, coinciding with the MMCT. This minimum is found in the study area around 14.1 Ma. Together, these data show some parallel variations between the inferred T_{air} in the north-east of the Iberian Peninsula, in the Ebro Basin, and T_{water} in palaeosols of Central Europe.

Regarding the timing of the onset and end of the MCO, there is a slight asynchrony in the beginning of warming

(onset of the MCO), with the warming in the lake system of this study manifesting *ca* 100 ka earlier than in the marine record (Figure 8F). Nevertheless, a longer delay might have existed if the age of *ca* 16.9 Ma is considered for the onset of warming, as identified by Holbourn et al. (2015) from benthic foraminifera and sediments in a Pacific core. As for the cooling following the MCO, the temperature gradually declined from *ca* 14.7 Ma in the marine record (Holbourn et al., 2014, 2015), some 100-150 ka before the sharp T_{air} drop detected in the study's lake basin (Figure 8B). Regarding the ending of the MCO, Methner et al. (2020) found a 300-ka offset between the palaeosol record in Central Europe (maximum at 14.9 Ma) and the bottom water temperatures (at 15.2 Ma), which was explained by a delay in the transmission of heat from the ocean to the atmosphere.

5.4 | Possible causes of the climate changes in the Iberian Peninsula

An array of interrelated factors coincided during the MCO, including orbital oscillations, changes in ocean heat transport, palaeogeography and atmospheric CO_2 (Holbourn et al., 2014, 2015; Steinthorsdottir et al., 2020), which make it difficult to know how global changes affected the studied lake basin. Changes in Antarctic ice sheet volume in conjunction with the $\delta^{13}C$ cycle alteration resulted in global changes in temperature and humidity. The position of the Iberian Peninsula and the general palaeogeography of the Ebro Basin (referred to its boundaries) during the MCO were the same as the present situation. Despite the array of factors that may have controlled climate changes during the Early and Middle Miocene, an increase of warm air masses entering the Iberian Peninsula during the MCO is expected. In this respect, it is worth noting that Baldassini et al. (2021) found that water in the western Mediterranean was warm from 17 to 14.55 Ma as a consequence of the closure, and partial reopening, of the Mediterranean Sea and the Indian Ocean. How much this situation affected the characteristics of the air masses on the Iberian Peninsula is unknown. It is likely that humid and cool air primarily from the Atlantic would have gained control from 14.5 Ma onwards.

6 | CONCLUSIONS

A lacustrine and distal alluvial record in north-east Iberia (17.73–14.0 Ma), encompassing the MCO, has been studied using sedimentological data and the $\delta^{18}O$ and $\delta^{13}C$ values of carbonate samples, and complemented by illite crystallinity index and MS data. Based on the results from the studied succession and their comparison with other continental and marine records, the following important points were made.

The onset of the MCO, at 17.10–17.06 Ma, has been inferred from an increase in T_{air}, humidity and chemical alteration, as well as a decrease in detrital magnetic-mineral concentration. This age is slightly older than the age reported in the marine record (17.0-16.9 Ma) for the onset of the MCO.

The end of the MCO, at 14.56 Ma, has been interpreted from a sharp increase in the P/E and cooling, a gradual fall in chemical alteration and an abrupt rise in detrital magnetic-mineral concentration. This age is slightly younger than that reported in the marine record (14.7 Ma) for the end of the MCO.

Through the MCO, variations in the studied parameters affecting humidity, temperature, chemical alteration and detrital supply have been noted, but their correlation with the marine MCO pattern is not straightforward. However, an interval of higher $\delta^{13}C$ values in the studied record, from 16.5 to 14.5 Ma, can be correlated with the Monterey excursion. Some intervals of temperature variations in the Ebro Basin record agree with similar variations identified in carbonate soils of Central Europe.

Of major significance is the finding that the multi-proxy analysis of this study supports the idea that some terrestrial environments, such as the lacustrine system in the Ebro Basin, have an earlier response to warming and a faster response to cooling than the marine realm. Moreover, lake records proved to be good for detecting some isotopic anomalies detected in ocean records, such as the Monterey $\delta^{13}C$ excursion.

CONFLICT OF INTEREST STATEMENT
The authors declare they have no affiliations with or involvement in any organisation or entity with financial or non-financial interest in the work submitted.

DATA AVAILABILITY STATEMENT

The data that support the findings of this study are available in the supplementary material of this article. Other data are available on request from the authors.

ORCID

Concha Arenas https://orcid.org/0000-0002-4212-0524

Cinta Osácar https://orcid.org/0000-0002-5246-366X

Francisco Javier Pérez-Rivarés https://orcid.org/0000-0002-9888-3539

Joaquín Bastida https://orcid.org/0000-0001-8051-6178

Andrés Gil https://orcid.org/0000-0001-6110-1081

Luis F. Auqué https://orcid.org/0000-0003-1463-1682

REFERENCES

Agustí, J., Pérez-Rivarés, F.J., Cabrera, L., Garcés, M., Pardo, G. & Arenas, C. (2011) The Ramblian-Aragonian boundary and its significance for the European Neogene continental chronology. Contributions from the Ebro Basin record (NE Spain). *Geobios*, 44(2–3), 121–134.

Alonso-Zarza, A.M. (2003) Palaeoenvironmental significance of palustrine carbonates and calcretes in the geological record. *Earth-Science Reviews*, 60(3–4), 261–298.

Alonso-Zarza, A.M., Meléndez, A., Martín-García, R., Herrero, M.J. & Martín-Pérez, A. (2012) Discriminating between tectonism and climate signatures in palustrine deposits: lessons from Miocene of the Teruel Graben, NE Spain. *Earth-Science Reviews*, 113, 141–160.

Arenas, C. (1993) Sedimentología y paleogeografía del Terciario del margen pirenaico y sector central de la Cuenca del Ebro (zona aragonesa occidental). PhD Thesis, Universidad de Zaragoza, https://zaguan.unizar.es/record/70725 (in Spanish)

Arenas, C., Casanova, J. & Pardo, G. (1997) Stable-isotope characterization of the Miocene lacustrine systems of Los Monegros (Ebro Basin, Spain): palaeogeographic and palaeoclimatic implications. *Palaeogeography Palaeoclimatology Palaeoecology*, 128, 133–155.

Arenas, C., Fernádez-Nieto, C., González-Pérez, J.M. & Pardo, G. (1993) Evolución mineralógica de los materiales miocenos de la Sierra de Alcubierre (sector central de la Cuenca del Ebro): Implicaciones en la evolución paleogeográfica. *Boletín de la Sociedad Española de Mineralogía*, 16, 51–64.

Arenas, C. & Pardo, G. (1999) Latest Oligocene–Late Miocene lacustrine systems of the north-central part of the Ebro Basin (Spain): sedimentary facies model and palaeogeographic synthesis. *Palaeogeography, Palaeoclimatology, Palaeoecology*, 151, 127–148.

Arenas, C. & Pardo, G. (2000) Neogene lacustrine deposits of the North-Central Ebro Basin, Northeastern Spain. In: Gierlowski-Kordesch, E.H. & Kelts, K.R. (Eds.) *Lake basins through space and time*. Tulsa, OK, USA: American Association Petroleum Geologists, Studies in Geology, vol. 46, pp. 395–406.

Arenas, C., Pardo, G., Pérez-Rivarés, F.J. & Vázquez-Urbez, M. (2007) From saline to freshwater lacustrine and fluvio-lacustrine carbonate systems: neogene evolution of the central Ebro Basin. In: Arenas, C., Alonso-Zarza, A.M. & Colombo, F. (Eds.) *Geological field trips to the lacustrine deposits of the northeast of*

Spain. Salamanca, Spain: Sociedad Geológica de España, 4th International Limnogeology Congress. Geo-Guías, 3, pp. 51–110.

Arkai, P. (1993) The distinction between low-T retrograde metamorphism and weathering plus burial diagénesis of the gneiss and mica schist basement-complex, Great Plain, Hungary—a novel use of illite crystallinity. *Neues Jahrbuch für Mineralogie-Monatshefte*, 8, 337–351.

Arostegi, J., Baceta, J., Pujalte, V. & Carracedo, M. (2011) Late Cretaceous—Palaeocene mid-latitude climates: Inferences from clay mineralogy of continental-coastal sequences (Tremp-Graus area, southern Pyrenees, N Spain). *Clay Minerals*, 46(1), 105–126. https://doi.org/10.1180/claymin.2011.046.1.105

Baldassini, N., Foresi, L.M., Lirer, F., Sprovieri, M., Turco, E., Pelosi, N. & Di Stefano, A. (2021) Middle Miocene stepwise climate evolution in the Mediterranean region through high-resolution stable isotopes and calcareous plankton records. *Marine Micropaleontology*, 167, 102030.

Bastida, J., Linares, R., López Buendía, A.M., Osácar, M.C., Rosell, J. & Zarroca, M. (2017) Weathering evolution in lutites of the K/Pg transition red beds of the Tremp Group (Tremp-Isona Basin, south Pyrenees). *Clay Minerals*, 52(1), 107–126. https://doi.org/10.1180/claymin.2017.052.1.08

Bauluz Lázaro, B., Arenas Abad, C., Fernandez-Nieto, C. & Gonzalez Lopez, J.M. (1994) Mineralogy and geochemistry of Miocene deposits at Alcubierre Sierra, central sector of the Ebro Basin, Spain. *Clay Minerals*, 29(3), 391–400. https://doi.org/10.1180/claymin.1994.029.3.10

Bohacs, K.M., Carroll, A.R., Neal, J.E. & Mankiewicz, P.J. (2000) Lake-basin type, source potential, and hydrocarbon character: an integrated sequence–stratigraphic geochemical framework. In: Gierlowski-Kordesch, E.H. & Kelts, K.R. (Eds.) *Lake Basins through space and time*. Tulsa, OK, USA: American Association Petroleum Geologists. vol. 46, 3–34.

Bohacs, K.M., Grabowski, G., Jr. & Carroll, A.R. (2007) Lithofacies architecture and variation in expression of sequence stratigraphy within representative intervals of the Green River Formation, Greater Green River Basin, Wyoming. *The Mountain Geologist*, 44(2), 39–58.

Böhme, M. (2003) The Miocene Climatic Optimum: Evidence from ectothermic vertebrates of Central Europe. *Palaeogeography, Palaeoclimatology, Palaeoecology*, 195(3–4), 389–401. https://doi.org/10.1016/S0031-0182(03)00367-5

Brandano, M., Cornacchia, I., Raffi, I., Tomassetti, L. & Agostini, S. (2017) The Monterey Event within the Central Mediterranean area: The shallow-water record. *Sedimentology*, 64(1), 286–310.

Bristow, T.F., Kennedy, M.J., Morrison, K.D. & Mrofka, D.D. (2012) The influence of authigenic clay formation on the mineralogy and stable isotopic record of lacustrine carbonates. *Geochimica et Cosmochimica Acta*, 90, 64–82.

Calvo, J.P., Daams, R., Morales, J., López-Martínez, N., Agustí, J., Anadón, P., Armenteros, I., Cabrera, L., Civis, J., Corrochano, A., Díaz-Molina, M., Elízaga, E., Hoyos, M., Martín Suarez, E., Moissenet, E., Muñóz, A., Pérez-Garcia, A., Pérez-González, A., Portero, J.M., Robles, F., Ruiz-Bustos, A., Santisteban, C., Torres, T., van der Meulen, A.J. & Vera, J.A. (1993) Up-to-date Spanish continental Neogene synthesis and paleoclimatic interpretation. *Revista de la Sociedad Geológica de España*, 6(3–4), 29–40.

Carroll, A.R., Chetel, L.M. & Smith, M.E. (2006) Feast to famine: sediment supply control on Laramide basin fill. *Geology*, 34, 197–200.

Casado, A.I., Alonso-Zarza, A.M. & La Iglesia, A. (2014) Morphology and origin of dolomite in paleosols and lacustrine sequences. Examples from the Miocene of the Madrid Basin. *Sedimentary Geology*, 312, 50–62.

Davis, B.L. & Smith, D.K. (1989) Table of experimental reference intensity ratios. *Powder Diffraction*, 3, 201–206.

Davis, S.J., Mulch, A., Carroll, A.R., Horton, T.W. & Chamberlain, C.P. (2009) Paleogene landscape evolution of the central North American Cordillera: developing topography and hydrology in the Laramide foreland. *Geological Society of America, Bulletin*, 121, 100–116.

Deocampo, D.M. (2010) The Geochemistry of Continental Carbonates. In: Alonso-Zarza, A.M. & Tanner, L.H. (Eds.) *Carbonates in continental settings: geochemistry, diagenesis and applications*. Amsterdam, *Developments in Sedimentology*, 62, 1–59: Elsevier. https://doi.org/10.1016/S0070-4571(09)06201-3

De Wet, C., Yocum, D.A. & Mora, C. (1998) Carbonate lakes in closed basins: sensitive indicators of climate and tectonics: an example from the Gettysburg Basin (Triassic), Pennsylvania, USA. In: Stanley, K.W. & McCabe, P.J. (Eds.) *Relative role of eustasy, climate and tectonism in continental rocks*, Vol. 59. Tulsa, OK, USA: SEPM, SpecialPublication, pp. 191–209.

Dworkin, S.I., Nordt, L. & Atchley, S. (2005) Determining terrestrial paleotemperatures using the oxygen isotopic composition of pedogenic carbonate. *Earth and Planetary Science Letters*, 237, 56–58. https://doi.org/10.1016/j.epsl.2005.06.054

Einsele, G. (2000) *Sedimentary basins: evolution, facies, and sediment budgets*. Heidelberg: Springer-Verlag, p. 792. https://doi.org/10.1007/978-3-662-04029-4

Ellwood, B.B., Crick, R.E., El Hassani, A., Benoist, S. & Young, R. (2000) Magnetosusceptibility event and cyclostratigraphy (MSEC) in marine rocks and the question of detrital input versus carbonate productivity. *Geology*, 28, 1135–1138.

Geiss, C.E., Umbanhowar, E., Camill, P. & Banerjee, S.K. (2003) Sediment magnetic properties reveal Holocene climate change along the Minnesota prairie-forest ecotone. *Journal of Paleolimnology*, 30, 151–166.

Gierlowski-Kordesch, E.H. (2010) Lacustrine carbonates. In: Alonso-Zarza, A.M. & Tanner, L.H. (Eds.) *Carbonates in continental settings: facies, environments and processes*. Amsterdam: Elsevier. *Developments in Sedimentology*, 61, 1–102.

Graf, J.W., Carroll, A.R. & Smith, M.E. (2015) Lacustrine sedimentology, stratigraphy and stable isotope geochemistry of the tipton member of the Green River Formation. In: Smith, M.E. & Carroll, A.R. (Eds.) *Stratigraphy and paleolimnology of the Green River Formation, Western USA*. Dordrecht: Springer. *Syntheses in Limnogeology*, 1, 31–60.

Grygar, T.M., Hošek, M., Mach, K., Schnabl, P. & Martínez, M. (2017) Climatic instability before Miocene Climatic Optimum reflected in a Central European lacustrine record from the Most Basin in The Czech Republic. *Palaeogeography, Palaeoclimatology, Palaeoecology*, 485, 930–945.

Hammarlund, D., Björck, S., Buchardt, B., Israelson, C. & Thomsen, C.T. (2003) Rapid hydrological changes during the Holocene revealed by stable isotope records of lacustrine carbonates from Lake Igelsjö n, southern Sweden. *Quaternary Science Reviews*, 22, 353–370.

Hamer, J.M.M., Sheldon, N.D., Nichols, G.J. & Collinson, M.E. (2007) Late Oligocene–early Miocene paleosols of distal fluvial systems, Ebro Basin, Spain. *Palaeogeography, Palaeoclimatology, Palaeoecology*, 247(3–4), 220–235.

Hammer, Ø., Harper, D.A.T. & Ryan, P.D. (2001) PAST: paleontological statistics software package for education and data analysis. *Palaeontologia Electronica*, 4(1), 1–9.

Harris, E.B., Kohn, M.J. & StroÅNmberg, C.A.E. (2020) Stable isotope compositions of herbivore teeth indicate climatic stability leading into the middle Miocene in Idaho. *Palaeogeography Palaeoclimatology Palaeoecology*, 546, 109610. https://doi.org/10.1016/j.palaeo.2020.109610

He, L., Liu, Z., Lyu, X. & Ma, P. (2022) Clay mineral assemblages of the oceanic red beds in the northern South China Sea and their responses to the Middle Miocene Climate Transition. *Science China Earth Sciences*, 65, 899–909. https://doi.org/10.1007/s11430-021-9878-0

Hirst, J.P.P. & Nichols, G.J. (1986) Thrust tectonic controls on Miocene alluvial distribution patterns, southern Pyrenees. In: Allen, P.A. & Homewood, J. (Eds.), *Foreland basins*, International Association of Sedimentologists, Spec Publ. 8, pp. 247–258.

Holbourn, A., Kuhnt, W., Schulz, M., Flores, J.A. & Andersen, N. (2007) Orbitally-paced climate evolution during the middle Miocene "Monterey" carbon-isotope excursion. *Earth and Planetary Science Letters*, 261(3–4), 534–550. https://doi.org/10.1016/j.epsl.2007.07.026

Holbourn, A., Kuhn, W., Lyle, M., Schneider, L., Romero, O. & Andersen, N. (2014) Middle Miocene climate cooling linked to intensification of eastern equatorial Pacific upwelling. *Geology*, 42, 19–22.

Holbourn, A., Kuhnt, W., Kochhann, K.G., Andersen, N. & Meier, K.S. (2015) Global perturbation of the carbon cycle at the onset of the Miocene Climatic Optimum. *Geology*, 43(2), 123–126. https://doi.org/10.1130/G36317.1

Holbourn, A.E., Kuhnt, W., Clemens, S.C., Kochhann, K.G.D., Jöhnck, J., Lübbers, J. & Andersen, N. (2018) Late Miocene climate cooling and intensification of southeast Asian winter monsoon. *Nature Communications*, 9, 1584. https://doi.org/10.1038/s41467-018-03950-1

Horita, J. (2014) Oxygen and carbon isotope fractionation in the system dolomite-water-CO_2 to elevated temperatures. *Geochimica et Cosmochimica Acta*, 129, 111–124. https://doi.org/10.1016/j.gca.2013.12.027

Jaboyedoff, M., Bussy, F., Kubler, B. & Thelin, P. (2001) Illite "crystallinity" revisited. *Clays and Clay Minerals*, 49(2), 156–167. https://doi.org/10.1346/CCMN.2001.0490205

Kelts, K. & Talbot, M.R. (1990) Lacustrine carbonates as geochemical archives of environmental change and biotic-abiotic interactions. In: Tilzer, M.M. & Serruya, C. (Eds.) *Large Lakes*. Heidelberg, Germany: Brock/Springer Series in Contemporary Bioscience. Springer-Verlag, Berlin, pp. 288–315.

Kürschner, W.M., Kvaček, Z. & Dilcher, D.L. (2008) The impact of Miocene atmospheric carbon dioxide fluctuations on climate and evolution of terrestrial ecosystems. *Proceedings of the National Academy of Sciences of the United States of America*, 105(2), 449–453. https://doi.org/10.1073/pnas.0708588105

Larena, Z., Arenas, C., Baceta, J.I., Murelaga, X. & Suarez-Hernando, O. (2020) Stratigraphy and sedimentology of distal-alluvial and lacustrine deposits of the western-central Ebro Basin (NE Iberia) reflecting the onset of the middle Miocene Climatic

Optimum. *Geologica Acta*, 18(7), 1–26, I–III. https://doi.org/10.1344/GeologicaActa2020.18.7

Lebreton-Anberrée, J., Li, S., Li, S.F., Spicer, R.A., Zhang, S.T., Su, T., Deng, C. & Zhou, Z.K. (2016) Lake geochemistry reveals marked environmental change in Southwest China during the Mid Miocene Climatic Optimum. *Science Bulletin*, 61(11), 897–910.

Leng, M.J. & Marshall, J.D. (2004) Palaeoclimate interpretation of stable isotope data from lake sediment archives. *Quaternary Science Reviews*, 23, 811–831.

Ma, P., Ma, C., Yang, S. & Fernandez, A.R. (2023) East Asian summer monsoon evolution recorded by the middle Miocene pelagic reddish clay, South China Sea. *Global and Planetary Change*, 222, 104072. https://doi.org/10.1016/j.gloplacha.2023.104072

McCrea, J.M. (1950) On the isotopic chemistry of carbonates and a paleotemperature scale. *The Journal of Chemical Physics*, 18(6), 849–857.

Maher, B.A. & Thompson, R. (Eds.). (1999) *Quaternary climates, environments and magnetism*. Cambridge: Cambridge University Press, p. 390. https://doi.org/10.1017/CBO9780511535635

Maher, B.A., Alekseev, A. & Alekseeva, T. (2003) Magnetic mineralogy of soils across the Russian Steppe: climatic dependence of pedogenic magnetite formation. *Palaeogeography, Palaeoclimatology, Palaeoecology*, 201, 321–341.

Mandic, O., de Leeuw, A., Vuković, B., Krijgsman, W., Harzhauser, M. & Kuiper, K.F. (2011) Palaeoenvironmental evolution of Lake Gacko (Southern Bosnia and Herzegovina): impact of the Middle Miocene Climatic Optimum on the Dinaride Lake System. *Palaeogeography, Palaeoclimatology, Palaeoecology*, 299, 475–592.

Martin-Bello, L., Arenas, C., Andrews, J., Alonso-Zarza, A.M. & Marca, A. (2019a) Multi-scale records of climate change in lacustrine stromatolites: insights from the Miocene Ebro Basin. *Palaeogeography, Palaeoclimatology, Palaeoecology*, 530, 312–329.

Martin-Bello, L., Arenas, C. & Jones, B. (2019b) Lacustrine stromatolites: useful structures for environmental interpretation—an example from the Miocene Ebro Basin. *Sedimentology*, 66, 2098–2133. https://doi.org/10.1111/sed.12577

Methner, K., Campani, M., Fiebig, J., Löffler, N., Kempf, O. & Mulch, A. (2020) Middle Miocene long-term continental temperature change in and out of pace with marine climate records. *Scientific Reports*, 10(1), 7989.

Mourik, A.A., Bijkerk, J.F., Cascella, A., Hüsing, S.K., Hilgen, F.J., Lourens, L.J. & Turco, E. (2010) Astronomical tuning of the La Vedova High Cliff section (Ancona, Italy)—Implications of the Middle Miocene climate transition for Mediterranean sapropel formation. *Earth and Planetary Science Letters*, 297, 249–261. https://doi.org/10.1016/j.epsl.2010.06.026

Muñoz, A., Arenas, C., González, A., Luzón, A., Pérez, A., Villena, J. & Pardo, G. (2002) Ebro Basin (northeastern Spain). In: Gibbons, W. (Ed.) *Moreno, T*. Geological Society of London: Geology of Spain, pp. 301–334.

Murray, S.T. & Swart, P.K. (2017) Evaluating formation fluid models and calibrations using clumped isotope paleothermometry on Bahamian dolomites. *Geochimica et Cosmochimica Acta*, 206, 73–93. https://doi.org/10.1016/j.gca.2017.02.021

Nichols, G.J. & Hirst, J.P. (1998) Alluvial fans and fluvial distributary systems, Oligo-Miocene, northern Spain; contrasting processes and products. *Journal of Sedimentary Research*, 68(5), 879–889.

Oerter, E., Amundson, R., Heimsath, A., Jungers, M., Chong, G. & Renne, P. (2016) Early to Middle Miocene climate in the Atacama Desert of Northen Chile. *Palaeogeography, Palaeoclimatology, Palaeoecology*, 441, 890–900.

Ogg, J.G. (2020) Geomagnetic polarity time scale. In: Felix, M., Gradstein, F.M., Ogg, J.G., Schmitz, M.D. & Ogg, G.M. (Eds.) *Geologic Time Scale*. Amsterdam, Netherland: Elsevier B.V., pp. 159–192.

Pavelić, D., Kovačić, M., Tibljaš, D., Galić, I., Marković, F. & Pavičić, I. (2022) The transition from a closed to an open lake in the Pannonian Basin System (Croatia) during the Miocene Climatic Optimum: Sedimentological evidence of Early Miocene regional aridity. *Palaeogeography, Palaeoclimatology, Palaeoecology*, 586, 110786.

Pérez Rivarés, F.J. (2016) Estudio magnetoestratigráfico del Mioceno del sector central de la Cuenca del Ebro: Cronología, correlación y análisis de la ciclicidad sedimentaria. PhD Thesis, University of Zaragoza. https://zaguan.unizar.es/record/79504 (in Spanish)

Pérez-Rivarés, F.J., Arenas, C., Pardo, G. & Garcés, M. (2018) Temporal aspects of genetic stratigraphic units in continental sedimentary basins: examples from the Ebro basin, Spain. *Earth-Sciences Reviews*, 178, 136–153.

Platt, N.H. (1989) Lacustrine carbonates and pedogenesis: sedimentology and origin of palustrine deposits form the Early Cretaceous Rupelo Formation, W Cameros Basin, N Spain. *Sedimentology*, 36, 665–684.

Pound, M.J., Haywood, A.M., Salzmann, U. & Riding, J.B. (2012) Global vegetation dynamics and latitudinal temperature gradients during the Mid to Late Miocene (15.97–5.33 Ma). *Earth Sciences Reviews*, 112, 1–22. https://doi.org/10.1016/j.earscirev.2012.02.005

Rhodes, M.K. & Carroll, A.R. (2015) Lake type transition from balanced-fill to overfilled: laney member, Green River Formation, Washakie Basin, Wyoming. In: Smith, M.E. & Carroll, A.R. (Eds.) *Stratigraphy and paleolimnology of the Green River Formation*. Western USA: Springer Dordrecht. *Syntheses in Limnogeology*, 1, 103–125.

Salvany, J.M. (1997) Continental evaporitic sedimentation in navarra during the oligocene to lower miocene: falces and Lerín Formations. In: Busson, G. & Schreiber, C. (Eds.) *Sedimentary deposition in rift and foreland basins in France and Spain (Paleogene and Lower Neogene)*. New York: Columbia University Press, pp. 397–411.

Sheldon, N. (2006) Using paleosols of the Picture Gorge Basalt to reconstruct the middle Miocene climatic optimum. *PaleoBios*, 26(2), 27–36.

Song, Y., Wang, Q., An, Z., Qiang, X., Dong, J., Chang, H., Zhang, M. & Guo, X. (2018) Mid-Miocene climatic optimum: clay mineral evidence from the red clay succession, Longzhong Basin, Northern China. *Palaeogeography, Palaeoclimatology, Palaeoecology*, 512, 46–55. https://doi.org/10.1016/j.palaeo.2017.10.001

Suarez-Hernando, O. (2017) Magnetobiocronología y paleoecología del Mioceno inferior-medio en las Bardenas Reales de Navarra (Cuenca del Ebro). PhD Thesis, Universidad del País Vasco/Euskal Herriko Unibertsitatea, 315 pp (in Spanish).

Sun, J. & Zhang, Z. (2008) Palynological evidence for the Mid-Miocene climatic optimum recorded in the cenozoic sediments of the Tian Shan Range, northwestern China. *Global and Planetary Change*, 64, 53–68.

Sreenivasan, S.P., Bera, M.K. & Samanta, A. (2023) A simple but improved protocol for measuring carbon and oxygen isotope ratios of calcite in calcite-dolomite mixtures. *Applied Geochemistry*, 150, 105600. https://doi.org/10.1016/j.apgeochem.2023.105600

Steinthorsdottir, M., Coxall, H.K., de Boer, A.M., Huber, M., Barbolini, N., Bradshaw, C.D., Burls, N.J., Feakins, S.J., Gasson, E., Henderiks, J., Holbourn, A.E., Kiel, S., Kohn, M.J., Knorr, G., Kürschner, W.M., Lear, C.H., Liebrand, D., Lunt, D.J., Mörs, T., Pearson, P.N., Pound, M.J., Stoll, H. & Strömberg, C.A.E. (2020) The Miocene: the future of the past. *Paleoceanography Paleoclimatology*, 36(4), e2020PA004037.

Talbot, M.R. (1990) A review of the palaeohydrological interpretation of carbon and oxygen isotopic ratios in primary lacustrine carbonates. *Chemical Geology (Isotope Geoscience section)*, 80, 261–279.

Talbot, M.R. & Kelts, K. (1990) Paleolimnological signatures from carbon and oxygen isotopic ratios in carbonates from organic carbon-rich lacustrine sediments. In: Katz, B.J. (Ed.) *Lacustrine basin exploration—case studies and modern analogs*, Vol. 50. Tulsa, OK, USA: American Association of Petroleum Geologists, Memoirs, pp. 99–112.

Thorez, J. (1989) Between crystal and the solution, a graphical overview of the passage to, from and of the clay minerals in the lithosphere during weathering. In: Barto Kiriakidis, A. (Ed.) *Weathering its products and deposits 1*. Athens: Teophrastus Publications, pp. 49–121.

Trayler, R.B., Kohn, M.J., Bargo, M.S., Cuitiño, J.I., Kay, R.F., Strömberg, C.A.E. & Vizcaino, S.F. (2020) Patagonian aridification at the onset of the Mid-Miocene Climatic Optimum. *Paleoceanography and Paleoclimatology*, 35, e2020PA003956. https://doi.org/10.1029/2020PA003956

Valero-Garcés, B.L., Delgado-Huertas, A., Navas, A., Machín, J., González-Sampériz, P. & Kelts, K. (2000) Quaternary palaeohydrological evolution of a playa lake: Salada Mediana, central Ebro Basin, Spain. *Sedimentology*, 47, 1135–1156.

Vázquez-Urbez, M., Arenas, C., Pardo, G. & Pérez-Rivarés, J. (2013) The effect of drainage reorganization and climate on the sedimentologic evolution of intermontane lake systems: the final fill stage of the Tertiary Ebro basin (Spain). *Journal of Sedimentary Research*, 83, 562–590.

Vincent, E. & Berger, W.H. (1985) Carbon dioxide and polar cooling in the Miocene: the Monterey hypothesis. In: *Sundquist, E.T. & Broecker, W.S. (Eds.), The carbon cycle and atmospheric CO_2: natural variations Archean to Present*. Geophysical Monograph Series, American Geophysical Union, Hoboken, NJ, USA: John Wiley & Sons; 32, 455–468. https://doi.org/10.1029/GM032p0455

Wang, Q., Song, Y. & Li, Y. (2020) Clay mineralogy of the upper Miocene-Pliocene red clay from the central Chinese Loess Plateau and its paleoclimate implications. *Quaternary International*, 552, 148–154. https://doi.org/10.1016/j.quaint.2019.11.039

Warshaw, C.M. & Roy, R. (1961) Classification and a scheme for the identification of layer silicates. *Geological Society of America Bulletin*, 72(10), 1455–1492. https://doi.org/10.1130/0016-7606

Westerhold, T., Marwan, N., Drury, A.J., Liebrand, D., Agnini, C., Anagnostou, E., Barnet, J.S.K., Bohaty, S.M., De Vleeschouwer, D., Florindo, F., Frederichs, T., Hodell, D.A., Holbourn, A.E., Kroon, D., Lauretano, V., Littler, K., Lourens, L.J., Lyle, M., Pälike, H., Röh, U., Tian, J., Wilkens, R.H., Wilson, P.A. & Zachos, J.C. (2020) An astronomically dated record of Earth's climate and its predictability over the last 66 million years. *Science*, 369(6509), 1383–1387. https://doi.org/10.1126/science.aba6853

Widera, M., Bechtel, A., Chomiak, L., Maciaszek, P., Stodkowska, B., Wachocki, R., Worobiec, E., Worobiec, G. & Zieliński, T. (2021) Palaeoenviromental reconstruction of the Konin Basin (central Poland) during lignite accumulation linked to the mid-Miocene climate optimum. *Palaeogeography, Palaeoclimatology, Palaeoecology*, 568, 110307.

Woodruff, F. & Savin, S. (1991) Mid-Miocene isotope stratigraphy in the deep sea: high resolution correlations, paleoclimatic cycles, and sediment preservation. *Paleoceanography*, 6, 755–806.

Yui, T.F. & Gong, S.Y. (2003) Stoichiometry effect on stable isotope analysis of dolomite. *Chemical Geology*, 201(3–4), 359–368. https://doi.org/10.1016/j.chemgeo.2003.08.007

Zachos, J., Pagani, M., Sloan, L., Thomas, E. & Billups, K. (2001) Trends, rhythms, and aberrations in Global climate 65 Ma to present. *Science*, 292, 686–693.

Zachos, J. .C., Dickens, G.R. & Zeebe, R.E. (2008) An early Cenozoic perspective on greenhouse warming and carbon-cycle dynamics. *Nature*, 451(7176), 279–283. https://doi.org/10.1038/nature06588

Zeng, M., Song, Y., An, Z., Hong, C. & Yue, L. (2014) Clay mineral records of the Erlangjian drill core sediments from the Lake Qinghai Basin, China. *Science China Earth Sciences*, 57, 1846–1859. https://doi.org/10.1007/s11430-013-4817-9

Zheng, D., Shi, G., Hemming, S.R., Zhang, H., Wang, W., Wang, B. & Chang, S. (2019) Age constrains on a Neogene tropical rainforest in China and its relation to the Middle Miocene Climatic Optimum. *Palaeogeography, Palaeoclimatology, Palaeoecology*, 518, 82–88.

SUPPORTING INFORMATION

Additional supporting information can be found online in the Supporting Information section at the end of this article.